Received: 23 December 2022 | Revised: 14 August 2023 | Accepted: 7 September 2023

DOI: 10.1111/gbi.12576

ORIGINAL ARTICLE

gebiology WILEY

Distinctive microfossil supports early Paleoproterozoic rise in complex cellular organisation

Erica V. Barlow[1,2,3] | Christopher H. House[3] | Ming-Chang Liu[4,5] | Maxwell T. Wetherington[6] | Martin J. Van Kranendonk[1,2]

[1]Australian Centre for Astrobiology, School of Biological, Earth and Environmental Sciences, University of New South Wales, Kensington, New South Wales, Australia

[2]Australian Research Council Centre of Excellence for Core to Crust Fluid Systems (CCFS), Macquarie University, Sydney, New South Wales, Australia

[3]Department of Geosciences and the Earth and Environmental Systems Institute, Pennsylvania State University, University Park, Pennsylvania, USA

[4]Department of Earth, Planetary, and Space Sciences, University of California at Los Angeles, Los Angeles, California, USA

[5]Lawrence Livermore National Laboratory, Livermore, California, USA

[6]Materials Research Institute and Department of Materials Science & Engineering, Pennsylvania State University, University Park, Pennsylvania, USA

Correspondence
Erica V. Barlow, Australian Centre for Astrobiology, School of Biological, Earth and Environmental Sciences, University of New South Wales, Kensington, NSW 2052, Australia.
Email: evbarlow@gmail.com

Funding information
Centre of Excellence for Core to Crust Fluid Systems, Australian Research Council; NASA Astrobiology; National Science Foundation

Abstract

The great oxidation event (GOE), ~2.4 billion years ago, caused fundamental changes to the chemistry of Earth's surface environments. However, the effect of these changes on the biosphere is unknown, due to a worldwide lack of well-preserved fossils from this time. Here, we investigate exceptionally preserved, large spherical aggregate (SA) microfossils permineralised in chert from the c. 2.4 Ga Turee Creek Group in Western Australia. Field and petrographic observations, Raman spectroscopic mapping, and in situ carbon isotopic analyses uncover insights into the morphology, habitat, reproduction and metabolism of this unusual form, whose distinctive, SA morphology has no known counterpart in the fossil record. Comparative analysis with microfossils from before the GOE reveals the large SA microfossils represent a step-up in cellular organisation. Morphological comparison to extant micro-organisms indicates the SAs have more in common with coenobial algae than coccoidal bacteria, emphasising the complexity of this microfossil form. The remarkable preservation here provides a unique window into the biosphere, revealing an increase in the complexity of life coinciding with the GOE.

KEYWORDS
great oxidation event, microfossil, Precambrian paleontology

1 | INTRODUCTION

The great oxidation event (GOE), ~2.4 billion years ago, represents an irreversible shift in atmospheric composition that dramatically altered weathering and nutrient cycles on the early Earth. Yet little is known about the effect of this change on the biosphere, as there is a worldwide scarcity of well-preserved fossiliferous rocks from this time period.

A well-preserved fossil deposit from this time period has recently been recognised within the lower part of the c. 2.4 Ga Turee Creek Group (TCG) in Western Australia. Work on this deposit has so far revealed a microbialite reef complex containing an assortment of very well-preserved macroscopic and microscopic fossils that provide unique insight into the diversity of life during the GOE (Barlow et al., 2016; Barlow & Van Kranendonk, 2018; Fadel et al., 2017; Nomchong & Van Kranendonk, 2020; Schopf et al., 2015). In particular, the appearance of the oldest known thrombolites and sideways branching stromatolites (Barlow et al., 2016; Nomchong & Van Kranendonk, 2020), two new microfossil forms (Barlow & Van Kranendonk, 2018) and the oldest known phosphorite (Soares et al., 2019), point to a link between the diversification of life and the rise of atmospheric oxygen.

Here, we provide a detailed morphological description and in situ carbon isotopic analyses of one of the new microfossil forms: a large spherical aggregate (SA) permineralised within nodular black chert (NBC). We combine field, petrographic and in situ carbon isotopic data to confirm the biogenicity of this unique fossil occurrence. We then interpret aspects of the SA microfossil morphology, assess its likely habitat and investigate its possible metabolism and reproduction. The remarkable preservation of the studied material reveals the SA microfossils constitute a form of cellular organisation previously unseen in rocks of this age, suggesting a possible link between the GOE and the development of more complex life.

2 | GEOLOGICAL SETTING

2.1 | Overview

The TCG is an approximately 4 km thick succession of metasedimentary rocks that crops out in the Hamersley Ranges of Western Australia, with its type locality in the Hardey Syncline (Figure S1). The group comprises, in ascending order, the Kungarra, Koolbye and Kazput formations (Thorne & Tyler, 1996), followed by the newly defined Munder and Anthiby formations (Figure S2; Martin, 2020). The TCG has experienced low-grade (prehnite-pumpellyite) burial metamorphism (Smith et al., 1982), with a maximum temperature estimated at between ~240°C and 280°C (Fadel et al., 2017; Williford et al., 2011).

The age of the TCG is constrained by the 2449 ± 3 Ma Woongarra Rhyolite of the conformably underlying Hamersley Group (Barley et al., 1997) and the 2209 ± 15 Ma Cheela Springs Basalt of the unconformably overlying Shingle Creek (previously lower Wyloo) Group (Martin et al., 1998; Figure S2). Detrital zircon geochronology and estimated sedimentation rates have been used to argue that the whole of the TCG was likely deposited by ~2.42 Ga (Krapez et al., 2017). This interpretation was disputed by subsequent studies that reported a ~2.3 Ga maximum age for the Meteorite Bore Member (MBM) diamictite of the Kungarra Formation (Caquineau et al., 2018; Philippot et al., 2018). However, a recent review questioned whether the ~2.3 Ga data represented a depositional age and concluded that the whole of the TCG, including the MBM, was most likely deposited between ~2450 and 2420 Ma (Bekker et al., 2020).

2.2 | Studied unit

The microfossil-bearing black chert studied here comes from within the upper stratigraphic portion of a well-preserved microbialite reef complex in the lower TCG (Barlow et al., 2016). This reef complex crops out on the faulted eastern limb of a tight, NW-plunging syncline within a coherent fold-train of Hamersley Group and TCG rocks (Figure S3). A minimum age for the reef complex has been obtained from two independent dates from euhedral apatite (c. 2.1–2.0 Ga), reflecting the timing of recrystallisation during regional metamorphism (Soares et al., 2019). The stratigraphic position of the microbialite reef complex is below the MBM, within the lower siliciclastic-dolostone member of the Kungarra Formation, confining its depositional age to c. 2.4 Ga during the earliest stages of the GOE (Bekker et al., 2020; Krapez et al., 2017; star within Figure S2).

The microbialite reef complex hosts a variety of shallow water dolomitic microbialites deposited in a setting that intermittently fluctuated between a restricted to semi-restricted lagoonal system and a more open ramp system (Barlow et al., 2016; Nomchong, 2021; Nomchong & Van Kranendonk, 2020). The shallow water portion of the reef complex is stratigraphically overlain by a deeper-water facies that contains dolosiltite, shale, ironstone and microfossiliferous nodular and bedded black chert units (Barlow et al., 2016; Barlow & Van Kranendonk, 2018).

2.2.1 | Sampling locality and description

The focus of this paper is the discovery of a novel type of large SA microfossil from cryptocrystalline black chert nodules that lie within shale at the base of an interbedded shale-ironstone-dolosiltite sequence (Barlow & Van Kranendonk, 2018). As part of a broader sampling campaign investigating the diversity of microfossils preserved at this locality, this interbedded shale-ironstone-dolosiltite sequence was mapped for ~12.5 km along strike, between 22°26.291′ S, 116°27.888′ E and 22°31.021′ S, 116°33.151′ E (white dots in Figure S3; Barlow, 2019). Chert samples were collected along the whole length of this sequence, including from the collection site of previous studies from where there is a break in the ridge colloquially known as the 'drive through' locality (Fadel et al., 2017; Schopf et al., 2015; white cross in Figure S3). The stratigraphy compiled from

10 transects across this deeper-water sequence by Barlow (2019) is summarised in Figure S4.

Black chert nodules occur over the transition between a ~0.5 and 1 m thick unit of fissile, grey weathering shale and an overlying, ~2 m thick, interbedded section of finely laminated silicified shale, ironstone and fine-grained bedded dolosiltite deposited as part of a regressive systems tract (Figure S4; Barlow et al., 2016). Black chert nodules are generally in the order of ~20 cm wide and ~7 cm high, but range to both smaller and larger sizes. Bedding bends down and around the curved underside of the nodules, indicating they were silicified before compaction accompanying lithification of this unit (Barlow & Van Kranendonk, 2018).

2.2.2 | Thin section description

In this study, SA microfossils are described from within eight thin sections created from four of the hand samples of NBC, collected from across ~12 km along strike. In thin section, these samples consist of a distinctive texture, termed *NBC texture 3* (Figure S5; Barlow, 2019; Barlow & Van Kranendonk, 2018). This texture typically contains abundant organic material, with large (hundreds of μm long) dense clumps that are elongated parallel to bedding and small (up to ~10–20 μm wide) fluffy clots that are distributed throughout. This texture also contains thick (~8–10 μm wide) filamentous microfossils (Figure S5c,d), as well as dispersed carbonate rhombohedra that are generally ≥100 μm wide along the short axis. *NBC texture 3* is distinct from the other microfossil assemblages previously described from separate samples of this nodular chert unit in the TCG microbialite reef complex: *NBC texture 1*, which contains an assortment of long filamentous, cob-web like microfossils of a benthic microbial community (Barlow, 2019; Barlow & Van Kranendonk, 2018; Fadel et al., 2017; Schopf et al., 2015), and *NBC texture 2*, which contains long, straw-like filamentous sheaths that encircle clusters of pyrite (Barlow, 2019; Barlow & Van Kranendonk, 2018).

3 | ANALYTICAL METHODS

3.1 | Petrographic microscopy

Images were captured on a Nikon Eclipse Ci POL microscope with a Nikon DS-Vi1 camera at the University of New South Wales. Both thick (~100 μm) and thin (~30 μm) sections of *NBC texture 3* (see Barlow, 2019; Barlow & Van Kranendonk, 2018) were studied using 5×, 10×, 20× and 50× oil-free magnification lenses under plane polarised light (PPL), cross polarised light (XPL) and reflected light (RL).

3.2 | Raman spectroscopy

Raman spectroscopy was undertaken in the Materials Characterization Laboratory in the Materials Research Institute at the Pennsylvania State University. Raman measurements were performed on a Horiba LabRam HR Evolution using a 532 nm excitation laser (Oxxious—LCX) with an incident power of 340 μW focused through a 100× (NA 0.9) objective lens. The spectrum was recorded with a 300 gr/mm grating and with a back-illuminated deep-depleted Si array detector (Horiba—Synapse). The spectrometer was calibrated using the spectral response of a single crystal Si sample (520 cm^{-1}). A low-resolution Raman map of a 20 × 50 μm area was acquired with 5 × 10 μm steps, with a 60-s integration time at each pixel in the map. The laser was focused through a 50× LWD (NA 0.5) objective lens and an incident power of 34 μW. A high-resolution Raman map was acquired with 0.9 integration second and step interval of 0.5 μm over a 12 × 20 μm area. A rendered image of the Raman spectral results was acquired by measuring the peak amplitude of the carbon (G band centred at ~1610 cm^{-1}) and quartz (centred 465 cm^{-1}) after correcting for the background.

3.3 | Confocal laser scanning microscopy

A confocal laser scanning microscope (CLSM) was used to image the SAs, both at the surface and at depth, to gain a sense of their three-dimensional nature and internal structure in a non-destructive manner. CLSM images were captured on an Olympus FV1200 microscope at the University of Cincinnati, using Olympus Fluoview software (version 3.1b). Limited fluorescence was produced from the large SA microfossils with excitation by the 458, 488, 515, 559 and 635 nm lasers, so reflected light was used instead. Images were obtained in 2D using the 488 nm laser at 10% power, with a 60× lens, a confocal aperture of 65 μm and no filter. These were then compared to transmitted light images of the same area to establish the amount of 'noise' in the images, in the form of scattered light from features in the adjacent material (as per Czaja et al., 2016). The amount of 'noise' was considered minor and thus, the 2D CLSM images displayed here are 'raw'.

3.4 | Secondary ion mass spectrometry

Two thin sections of *NBC texture 3* were viewed on a petrographic microscope under both PPL and RL to find areas where several microfossils were exposed at the surface, from which three small (~5 mm^2) regions of interest (ROIs) were selected for in situ carbon isotope analyses. ROIs (labelled 318Fv3_01, 318Fv3_02 and 318Fv2) were removed from the thin sections using a diamond-tipped glass cutter, then each ROI chip was mapped in both PPL and RL.

Composite sample pucks (labelled C01, C02 and C03) were created with each puck containing ROI chip/s and a small (<5 mm^2 at surface) piece of carbon standard ('PEEK'; $\delta^{13}C_{VPDB}$ value of −27.7‰; House, 2015; Oehler et al., 2017). Each puck was sonicated sequentially: three times each for 1 min in deionised water, followed by 30 s in ethanol and again twice each for 30 s in deionised water. Sample pucks were then dried with a stream of high purity nitrogen and placed in a

60°C vacuum oven overnight to degas. Before analysis, sample pucks were gold coated and placed in a 60°C vacuum oven for 48 h.

In situ carbon isotope measurements of microfossils were carried out in multi-collection mode ($^{12}C^{12}C^-$ on an off-axis Faraday cup and $^{12}C^{13}C^-$ on the axial electron multiplier) using a CAMECA-IMS 1290 secondary ion mass spectrometer (SIMS) at the University of California, Los Angeles. Carbon standards were presputtered using a 400-pA beam, followed by carbon isotope measurement using a 100-pA primary ion beam for 30 cycles. Due to differences in count rate (i.e. carbon signal), a greater beam intensity was used to measure the carbon isotope ratios of sample material than for carbon standards. TCG chert samples were presputtered for 90 s using a 400-pA beam, followed by carbon isotope measurement using either a 400 pA, 1 or 3 nA primary ion beam for up to 30 cycles. Internal precision is defined as one standard error ($\pm 1\sigma$) of each measurement.

To account for the deviations from the true isotope ratio caused by instrumental mass fractionation and the difference in detector gains/yields, a bias factor (α) was calculated using Equation (1), where $\delta^{13}C_{obs\_std}$ is the weighted mean raw (observed) value of the standard measured during a single SIMS session, and the $\delta^{13}C_{exp\_std}$ is the true (expected) value of the standard measured externally by a gas-source mass spectrometer in relation to Vienna Pee Dee Belemnite (VPDB). The standard used in this case was a synthetic carbon standard called 'PEEK', which has a true $\delta^{13}C_{VPDB}$ value of −27.7‰ (House, 2015; Oehler et al., 2017).

$$\alpha = \frac{(\delta^{13}C_{obs\_std} + 1000)}{\delta^{13}C_{exp\_std} + 1000} \quad (1)$$

The bias factor (α) was then used to determine the corrected ('true') $\delta^{13}C$ value of TCG samples using Equation (2), where $\delta^{13}C_{obs\_sam}$ is the raw value of the sample measured by SIMS.

$$\delta^{13}C_{true\_sam}\,(‰) = \left[\frac{(\delta^{13}C_{obs\_sam} + 1000)}{\alpha}\right] - 1000 \quad (2)$$

4 | RESULTS

4.1 | Key morphologic and petrographic observations

The forms described here are spherical to slightly ellipsoidal-shaped aggregates (Figures 1–3) whose three-dimensionality was evidenced by varying the focal depth within thick sections (~100 μm) under the petrographic microscope. The SA microfossils range in size from ~52 to 162 μm in diameter, with most specimens between ~83 and 110 μm diameter (mean = 97 μm, measured population = 59; Figure S6a,b). They are preserved as distinct, individual forms, with some specimens locally occurring in relatively close proximity (Figure 2a–d), but most are widely scattered throughout a section (e.g. Figure S10). Previous, preliminary work showed the SA microfossils have a kerogenous composition (Barlow & Van Kranendonk, 2018), which we confirm with additional Raman spectroscopic analysis here (Figure 4a–c).

Sixty per cent of measured specimens are surrounded by a distinctive rind that forms a prominent, optically clear, circular halo visible in thin section (Figures 1–3). These rinds are free of the fluffy, particulate organic matter (OM) that fills the matrix of studied samples, but high-resolution Raman mapping shows the optically clear rinds do contain sub-micron-sized kerogen embedded within the quartz (Figure 4a,d,e). Rinds are, on average, ~20 μm wide (Figure S6c,d) and are composed of fine-grained microquartz that is either the same size as (Figure 1c), or much finer-grained than (Figure 1e), the microquartz that preserves the fluffy OM in the matrix. About 30% of measured specimens have a carbonate (calcite) rhomb directly associated with them—either touching the main spheroidal body, or poking into the clear rind (e.g. Figures 1a–c,e and 2b,e).

Some SA microfossils lie on a layer of concentrated OM that deflects downwards, partly around the stratigraphic underside of the fossil (Figures 1a, 2d, and 3d; Figure S7). In these cases, the SA rind varies from being either an even thickness the whole way around the aggregate (e.g. Figure 1a) or thinned on the stratigraphic underside of the aggregate and bulged around the stratigraphic topside (e.g. Figure 2d; Figure S7c,d).

The outer portion of the organic body of the SA microfossils has an irregular edge, with jagged to wispy wire-like structures that poke out into the clear rind (Figures 1–3). In some places, these structures are intricately bent and twisted and extend out into the clear rind up to 15 μm further than the rest of the main spheroidal body (e.g. Figure 3a).

Internally, the SAs consist of a honeycomb-like framework of sub-spherical to slightly polygonal compartments composed of granular, dark brown- to black-coloured OM (e.g. clearly visible in Figures 1d and 3b). The compartments are densely packed, which makes it difficult to definitively determine their diameter or the number of compartments per microfossil. However, most SAs were observed to contain at least 20 compartments, ranging from ~12 to 17 μm (av. 15 μm) wide. In some SA specimens, the compartments are present only around the perimeter of the microfossil, creating the appearance of a hollow core (e.g. Figure 3a, Figure S12e–h).

In several specimens, amber brown-coloured cell-like spheres fill the honeycomb-like compartments (Figures 5 and 6). These cell-like spheres are generally ~11 μm diameter, commonly contain clear central domains and are distinct in colour and texture from the surrounding compartment walls (Figures 5d,e,g and 6c–g,j). In one specimen, multiple tightly packed cell-like spheres as small as ~3.5 μm diameter were observed within a single compartment (Figure 6c,e).

4.2 | In situ carbon isotopes

In situ carbon isotopic data were obtained from the SAs and associated OM within the chert matrix of *NBC texture 3* samples

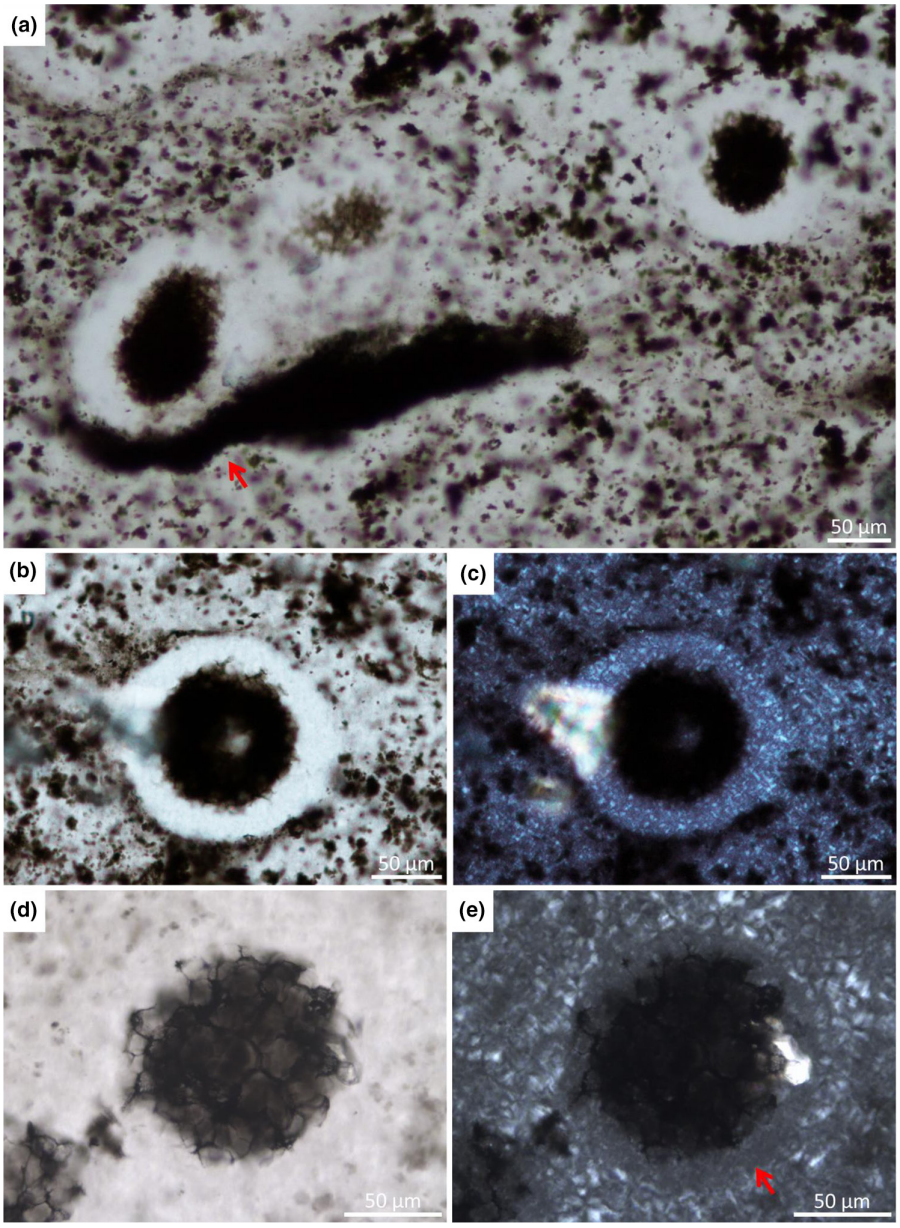

FIGURE 1 Archetypal large spherical aggregate (SA) microfossils with wide, kerogen-free surrounding rinds. Microfossil shape is most commonly spherical, with radial symmetry. All images are vertical cross sections through bedding. (a) Plane polarised light (PPL) image of slightly ellipsoidal SAs oriented with long axes perpendicular to bedding; note the even width of rinds. Dense, bedded organic matter (OM) that directly underlies the left SA appears to be deflected downwards, around the SA and its surrounding rind (arrow). (b, c) and (d, e) show specimens in both PPL and cross polarised light (XPL), highlighting the very fine microquartz grainsize within the rinds (arrow in e). Carbonate rhombs are occasionally observed intruding into microfossil rinds; these are visible in a (left SA, right side of rind), in b, c (left side of rind), and in e (right side of rind).

(Figures S8–S16; Tables S1–S4). SA $\delta^{13}C$ values spanned −32.2‰ to −24.6‰, with a weighted mean $\delta^{13}C$ of −30.4 ± 2.3‰ ($n = 19$; Figure 7). Variations in the carbon isotopic composition of specific features within the SAs (e.g. wispy wire-like structures, compartment walls or cell-like spheres) could not be resolved, as these features were too closely spaced to be individually distinguished using the ion microprobe beam (e.g. see Figures S11, S12, and S14).

Within the chert matrix, the dense, bedded OM and fluffy-looking OM clots collectively recorded a lighter range of $\delta^{13}C$ values (−37.2 to −29.1‰; w. mean −31.8 ± 2.2‰; $n = 12$; Figure 7), with the lightest value coming from OM that forms a partial rim around the outside of a SA rind ($\delta^{13}C$ −37.2 ± 0.6‰; Figure S12). (For the definition of w. mean as used here, see Table S1.)

5 | DISCUSSION

5.1 | Syngeneity and biogenicity

The syngeneity and biogenicity of the SAs have briefly been discussed previously (Barlow & Van Kranendonk, 2018), but here we provide a more complete assessment of each.

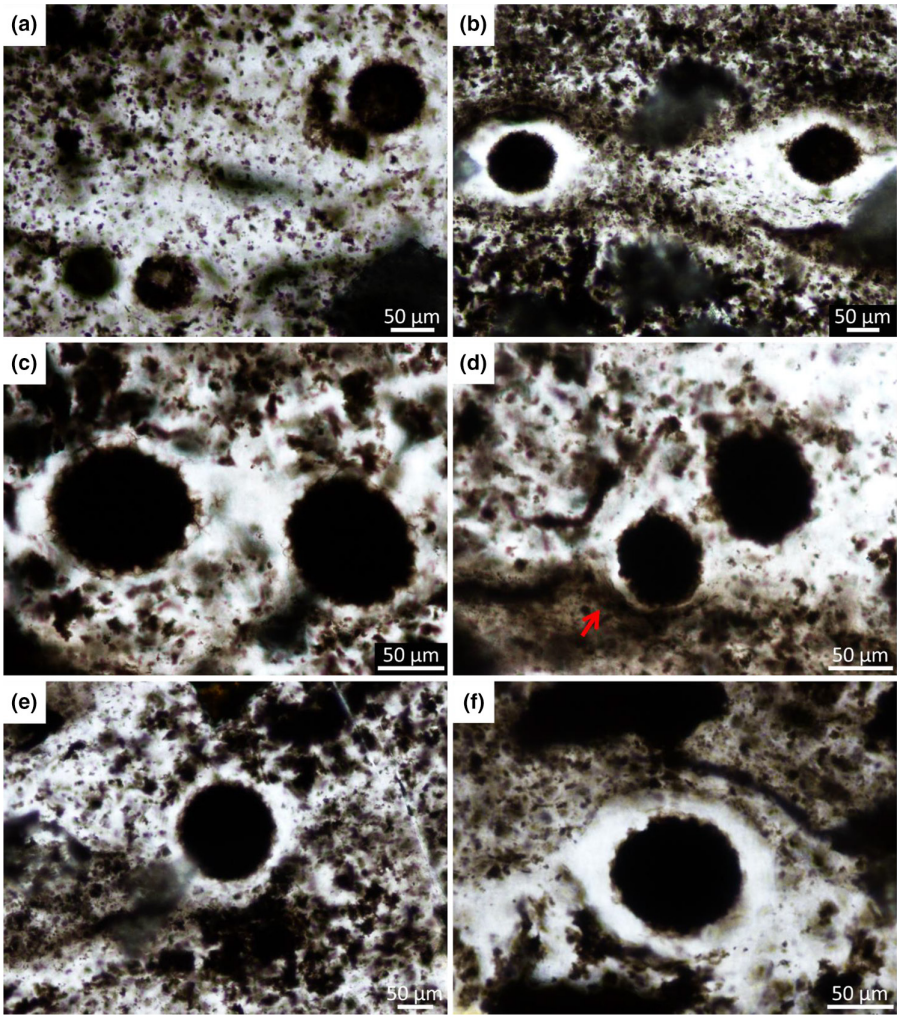

FIGURE 2 SA microfossils appear as individual specimens of consistent size and shape and are occasionally observed in relatively close proximity. The main organic 'body' of the SAs has an irregular edge, with thin, wispy, wire-like structures that extend out into the clear surrounding rind (most clearly visible in c). Note the transparent calcite rhombs poking into the SA rinds in (b) and (e). Arrow in (d) highlights deformed OM that bends around the underside of the SA; note the SA rind here is uneven (thin on the underside and thick on the topside; see also Figure S7d). All images are vertical cross sections through bedding in PPL, taken from thick (~100 μm) petrographic sections. The thickness of the section combined with the density of surrounding OM obscures the SA rind in places.

Firstly, the syngeneity of the SAs and associated OM in nodular chert samples is demonstrated by:

- the lack of a magmatic component in the TCG that could have produced (and/or subsequently transported) abiotic OM (cf. Thorne & Tyler, 1996);
- the absence of hydrothermal or cross-cutting veins associated with TCG black chert samples at outcrop scale, precluding OM having been supplied into the chert nodules at a later time;
- the absence of any indication of fluid/oil migration or large-scale redistribution of OM at either hand sample or thin section scale (e.g. Rasmussen et al., 2021);
- the fact that the chert nodules themselves formed very early, pre-compaction of the surrounding sediments (evidenced by the way the surrounding carbonate and shale layers bend around the nodules; see fig. 2d of Barlow & Van Kranendonk, 2018), showing that their contained OM was also preserved early and cannot have formed from later input; and
- the fact that the SAs were clearly preserved in place before minor (sub-mm-scale) quartz fractures (e.g. see cross-cutting relationships in Figures S8, S10 and S13).

Combined, these details show that the SAs and associated OM are indigenous to, and are the same age as, the surrounding rock in which they are encased.

Secondly, multiple lines of evidence (modified after Brasier et al., 2004) demonstrably establish the SAs as bona fide, biogenic microfossils, as they:

- occur in a geological context plausible for life, that is, within sedimentary rocks formed in a marine setting that were subjected only to relatively low-grade burial metamorphism, with

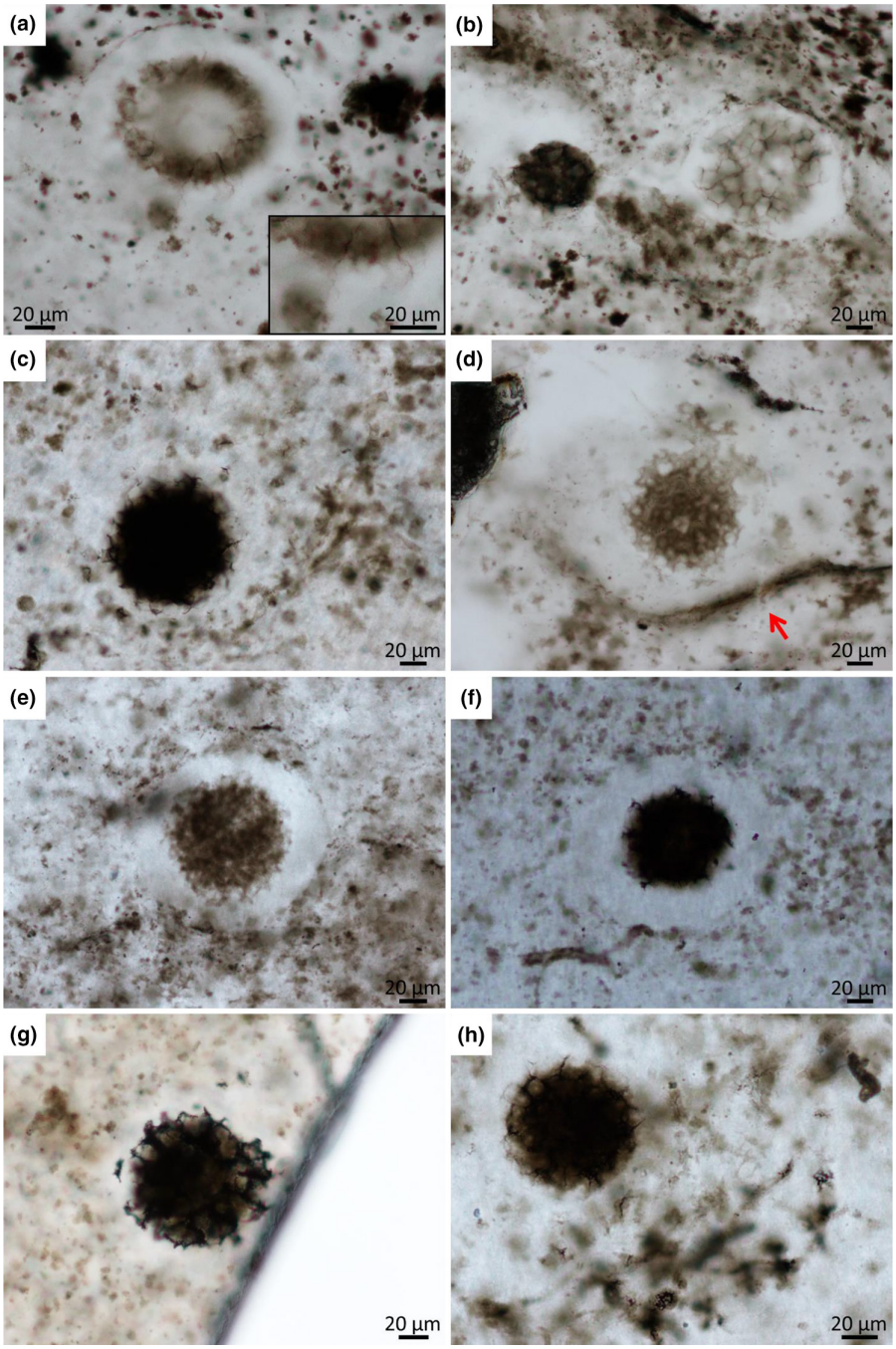

FIGURE 3 In thinner (~30 μm thick) petrographic sections, SA microfossils are more transparent, revealing an internal framework of honeycomb-like compartments. The compartments are sub-spherical to polygonal in shape and are composed of dark brown, often granular, OM. (a) SA specimen with a hollow core and an even rind that is partially outlined along the outer, top edge. Inset shows enlarged view of thin, wispy structures emanating out from the SA body into the surrounding rind. (b–h) Variably preserved SA microfossils and surrounding rinds. Arrow in (d) points to deflected underlying bedding (see also Figure S7). Fragments of thick filamentous microfossils are visible in (f) and (h). The line in (g) that cuts diagonally across the image is the broken edge of the thin section. All images are vertical cross sections through bedding in PPL.

temperatures not exceeding ~240 to 280°C (Fadel et al., 2017; Williford et al., 2011). This setting and history are inconsistent with abiological formation of OM through high-temperature mineralisation (i.e. ~500°C; Garcia-Ruiz et al., 2003) or Fischer-Tropsch-type synthesis (e.g. McCollom et al., 1999), and are also inconsistent with pseudo-fossil formation through localised mobilisation of OM, as this has been described from rocks that have experienced extensive, syn-sedimentary hydrothermal input and subsequent high-temperature (~350°C) metamorphism (e.g. Coutant et al., 2022);

- occur in a stratigraphic sequence with other fossils of unambiguous origin, that is, multiple varieties of microbialites (Barlow

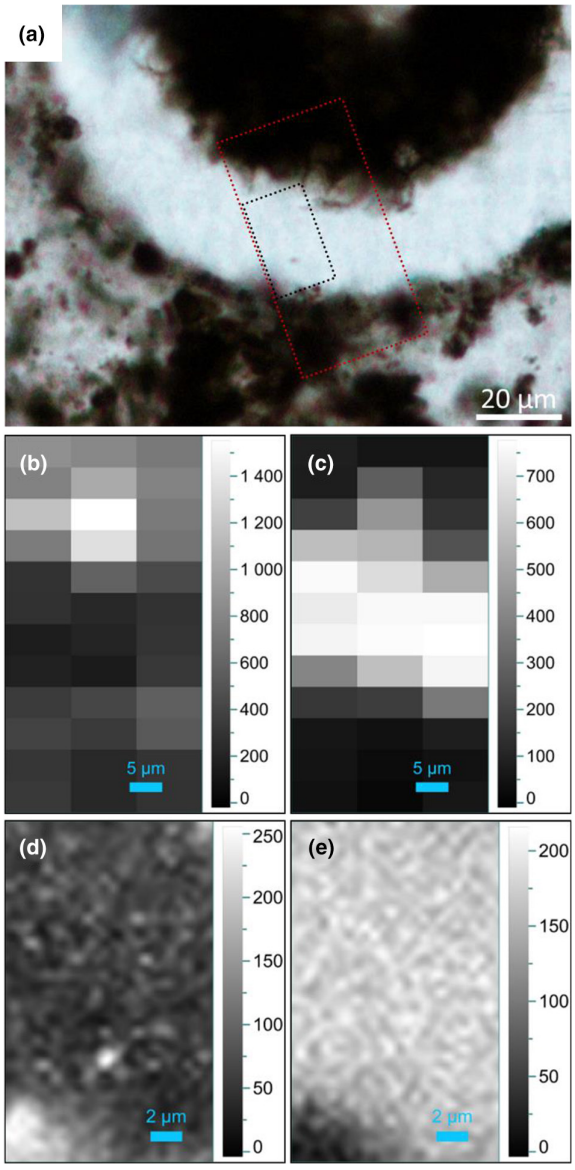

FIGURE 4 Raman mapping of a SA microfossil, its rind and the organic material of the surrounding matrix. (a) Close-up of a SA microfossil specimen with dashed boxes showing the location of Raman maps b/c (red box) and d/e (black box). This is the same SA specimen as shown in Figure 1b. (b, c) Low magnification and (d, e) high magnification maps of the regions shown in (a), displaying carbon (parts b, d) and quartz (parts c, e) distribution. The greyscale bars in parts (b) and (d) reflect the relative intensity of the carbon peak (G band, centred at ~1610 cm^{-1}), and those in parts (c) and (e) depict the relative intensity of the quartz peak (centred at ~465 cm^{-1}).

et al., 2016; Nomchong & Van Kranendonk, 2020) and other bona fide microfossils with cellular preservation (Barlow & Van Kranendonk, 2018; Fadel et al., 2017; Schopf et al., 2015);

- occur within multiple petrographic thin sections produced from different samples that were collected from kilometres apart along strike;
- occur in a distinct and repeated microfossil assemblage (termed *NBC texture 3*; Barlow & Van Kranendonk, 2018; Barlow, 2019) alongside other kerogenous microfossils of markedly different, filamentous morphotype (Figure S5c,d);
- each have a three-dimensional morphology of consistent size and shape (Figures 1–3; Figure S6);
- exhibit both a morphology and size range that is consistent with that known to be produced by life (see Section 5.2.3);
- are of kerogenous composition and are not composed of any minerals other than the microquartz in which they are preserved (Figure 4; see also Barlow & Van Kranendonk, 2018); and
- have an in situ carbon isotopic composition that is consistent with biological fractionation ($\delta^{13}C$ of ~ −30‰; Hayes et al., 1999).

5.2 | Microfossil analysis

Most biological information (e.g. physiological, genetic, biochemical, reproductive, ecological) is typically not preserved in fossilised micro-organisms from ancient rocks. Usually, only the morphology and basic chemical information are retained and available for investigation (Knoll, 2014). This data paucity means that microfossil characterisation is largely reliant on the interpretation of morphological and contextual observations, as well as morphological comparison to modern forms (Golubic & Barghoorn, 1977); we thus use such an approach in our investigations here.

5.2.1 | Interpretation of morphological and contextual observations

Timing of silicification

As outlined above (see Section 2.2.1), field observations indicate that the chert nodules were silicified during early diagenesis, prior to compaction from the overlying sediments. More specifically, in order to preserve the SA microfossils, the filamentous microfossils and the variation in the morphology and texture of the matrix-filling OM, silicification of the nodules must have initiated very early, as microbial decomposition can occur within the timeframe of days to weeks (Bartley, 1996). Very early silicification is supported by observations of the consistently spherical shape of both the SAs and their surrounding rinds, despite being located among beds of dense OM that are flattened along bedding planes (e.g. Figure S8 and Figure 10). Where the shape of the SAs and their surrounding rinds is ellipsoidal, the long axis is either parallel to (Figure 2b) or, more commonly, perpendicular to (Figure 1a; Figure S7a,b) bedding. This shows that the microfossils were not affected by widespread compaction-related deformation, supporting very early silicification of this material.

Clear outer rinds

Clear outer rinds are unusual but are not unknown from the fossil record. They have been documented in fossilised micro-organisms from younger deposits and have been variously interpreted as being of diagenetic origin (Anderson et al., 2019; Xiao et al., 2000),

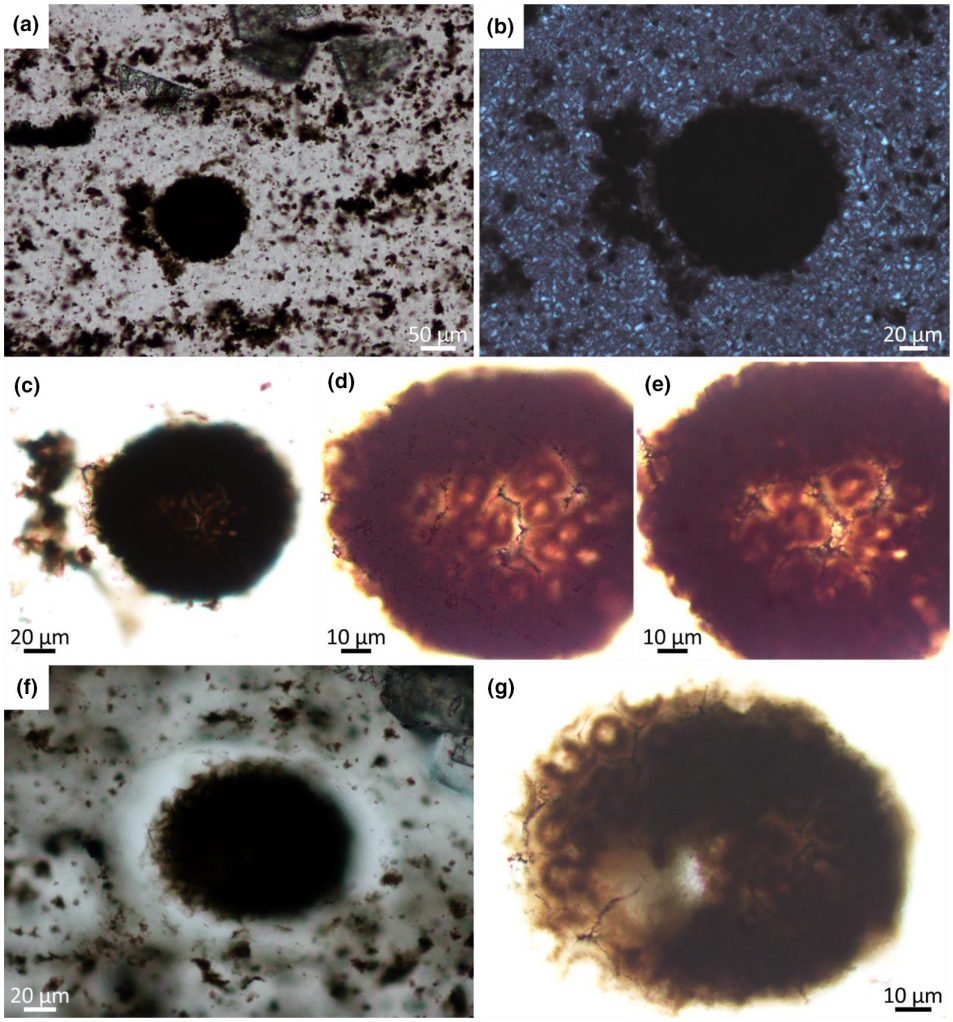

FIGURE 5 Well-preserved SA microfossils contain amber brown-coloured cell-like spheres within the honeycomb-like compartments. (a, b) Dense, opaque SA specimen in PPL (a) and XPL (b). Part b shows the fine-grained microquartz that preserves the SA. (c–e) Same specimen as a/b imaged under higher magnification and overexposed to more clearly show the internal structure (d and e are taken in the same x/y position but at different focal depths). Note the darker, more granular nature of the honeycomb-like compartments that surround the cell-like spheres. (f) Another opaque SA specimen in PPL; note the thin wispy structures that extend out into the kerogen-free rind. (g) Same specimen as in f, overexposed to show it is composed of tightly packed cell-like spheres that are distinct from the honeycomb-like framework. Note the clear central domains within the cell-like spheres in (d), (e) and (g).

taphonomic origin (Jing et al., 2022), or the remains of something inherent to the original micro-organism (Kazmierczak & Kremer, 2009; Sergeev, 1994).

A diagenetic origin has been proposed for the clear outer rinds in acritarch microfossils described from Ediacaran phosphorites (Anderson et al., 2019; Xiao et al., 2000). This is due to the orientation and isopachous nature of acicular apatite crystals in the rind that indicate nucleation on, and subsequent growth outwards from, the cell wall (see fig. 1e–h of Xiao et al., 2000). Although this example involves a different mineral to that studied here (i.e. apatite as opposed to quartz), a similar process could have occurred in our samples via a silica mineralisation front pushing OM away from the SAs. Such a process has been demonstrated in an artificial fossilisation experiment by Oehler (1976), who documented that fibrous, radiating, spherulitic quartz precipitated outwards from an OM-rich nucleation site and pushed OM ahead of the growth front. This experiment resulted in a ~7–12 µm thick halo of clear quartz around the nucleation site and a ~2.5 µm thick rim of concentrated OM around the outside of the halo (see fig. 5j of Oehler, 1976). However, we regard this explanation for the formation of the SA rinds as unlikely, as characteristics of this process (i.e. fibrous or radiating spherulitic quartz and a dense concentration of OM around the outside of the entire rind) are not present in the studied microfossils (Figure 1).

Taphonomic experiments on extant micro-organisms have established that cellular contents can shrink dramatically due to water loss during decomposition (Golubic & Hofmann, 1976; Knoll & Barghoorn, 1975). It is therefore plausible that shrinkage could explain the occurrence of clear outer rinds described in microfossils from other deposits. For example, Jing et al. (2022) documented single spheroidal bodies of variable size and shape, each surrounded by a clear rind either with, or without, an opaque cell wall on the outside

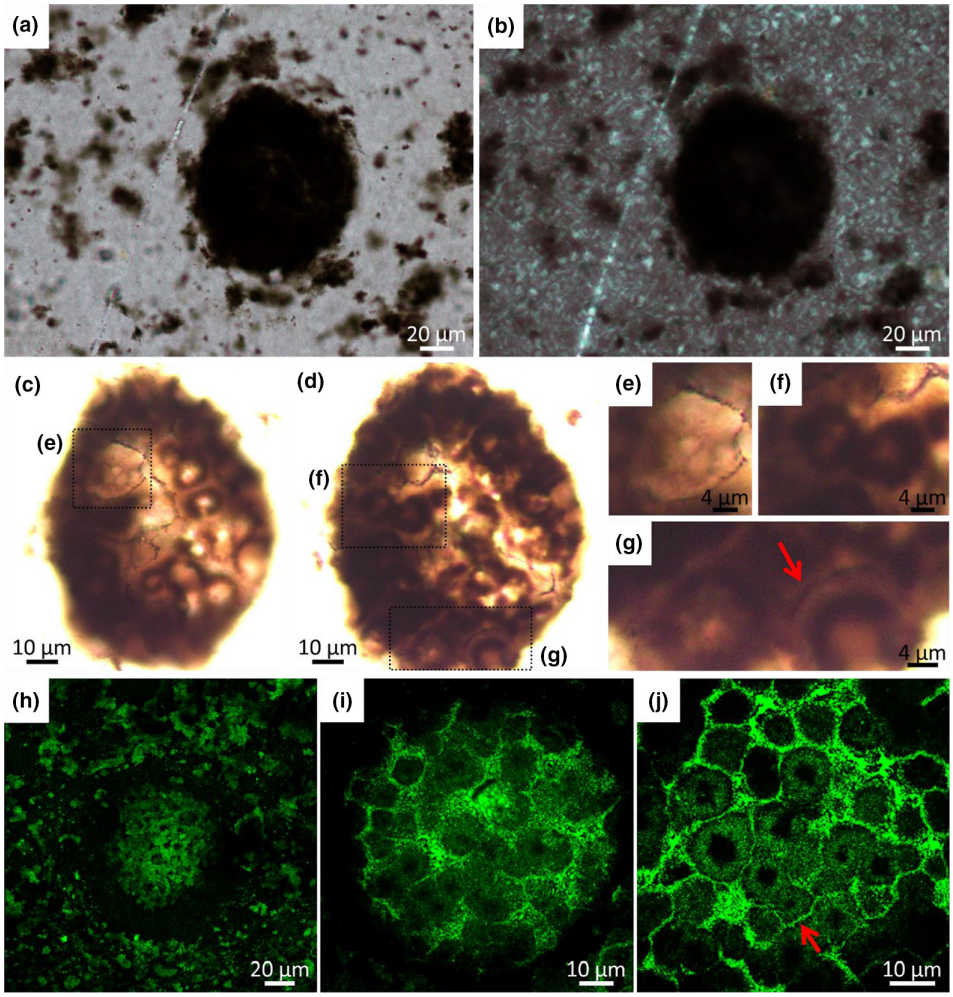

FIGURE 6 Internal structure of the SA microfossils, continued. (a, b) Opaque SA microfossil in PPL (a) and XPL (b), highlighting the consistent size of the microquartz preserving the microfossil. (c–g) Higher magnification images in PPL of same specimen as in a/b; Images are overexposed to show internal detail more clearly. Parts (c) and (d) are taken in the same x/y position but at different focal depths, highlighting the tightly packed cell-like spheres contained within the SA. Part (e) is detail of boxed area in (c), showing what appear to be multiple, smaller cell-like spheres contained within one compartment. At least five cell-like spheres are visible, and these are ~3.5 to 4 μm in diameter. Parts (f) and (g) show detail of boxed areas in (d), indicating the spherical nature of the cell-like spheres (f) and that they appear to be separate from the OM of the surrounding compartments (arrow in g). (h–j) Confocal laser scanning microscope (CLSM) images of SA microfossils. Note the clear rind visible in (h), and the spherical to polygonal compartments in (j) (arrow). Also note the clearer central domains within the cell-like spheres (visible in c, f, g, j). Parts (a), (h), (i) and (j) are of different specimens.

of the rind (see figs. 10 and 11 of Jing et al., 2022). The variability in size and shape of these spheroidal bodies is fully consistent with shrinkage during decomposition (Golubic & Hofmann, 1976; Knoll & Barghoorn, 1975).

It is likely that some shrinkage may have occurred during decomposition of the SA microfossils described here prior to silicification. However, a taphonomic *origin* for the clear rind is unlikely, as this would require the SAs to have had an outer cell wall to hold back the OM in the surrounding matrix. Although we have observed one specimen that contains what could be the remains of a partial cell wall (Figure 3a), this feature has not consistently been observed in the specimens here (Figures 1, 2, and 3b–h). Moreover, SA size does not vary with the presence or absence of a rind: the mean diameter of SAs with a rind is 96.7 μm and those without is 97.6 μm (Table S5). This indicates that, if shrinkage occurred in the SAs, it was independent of the presence/absence of a rind, suggesting taphonomy alone cannot explain the formation of the rind here.

Instead, morphological comparison with extant and fossilised micro-organisms suggests that the clear rind could derive from an original feature of the SA micro-organism. Many extant micro-organisms, particularly colonial forms, contain thick mucilaginous membranes that provide a wide, physical barrier between the cells and the outside world (Figure 8a; Komarek & Johansen, 2015; Matthews, 2016; Nakada & Nozaki, 2015). Mucilaginous membranes have also been documented in younger fossilised micro-organisms that have distinctive, clear outer rinds (Figure 8b; Kazmierczak & Kremer, 2009; Sergeev, 1994). There are marked similarities between these modern and fossilised mucilaginous membranes and the relative size, shape and structure of the clear rind around the SAs, including in the appearance of holding back surrounding particles (cf. Figures 1a,b and 8a). Based on these examples,

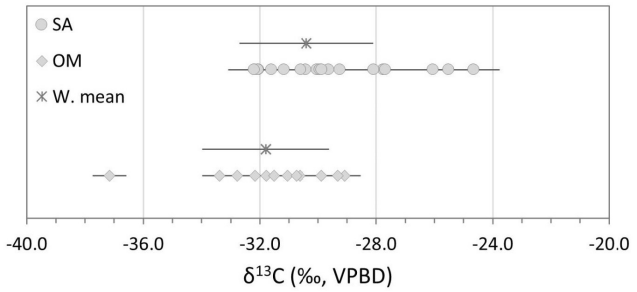

FIGURE 7 In situ carbon isotope results from nodular black chert samples (NBC texture 3 of Barlow, 2019; Barlow & Van Kranendonk, 2018). SA microfossil data are depicted by circles (asterisk above SA data set is w. mean: $\delta^{13}C$ −30.4 ± 2.3‰; $n = 19$). Data collected from the dense and fluffy OM were combined and are displayed here as diamonds (asterisk above OM data set is w. mean: $\delta^{13}C$ −31.8 ± 2.2‰; $n = 12$). For definition of w. mean, see Table S1. Grey bars in main data sets indicate error (for individual measurement errors, see Tables S2–S4). Grey bars for weighted means = 1SD.

we interpret the clear rind around the SA microfossils as a silicified mucilaginous membrane.

This interpretation is supported by high-resolution Raman mapping of a SA rind, which shows the optically clear rind is composed of sub-micron-sized kerogen (Figure 4a,d,e). The presence of a calcite rhomb in close spatial association with ~30% of SA specimens may also support this interpretation, as the degradation of extracellular polymeric substances (EPS) is known to result in calcite mineralisation (Dupraz & Visscher, 2005, and refs therein). Moreover, the observation of microquartz in some SA rinds being distinctly finer grained than that in the surrounding chert matrix (e.g. Figure 1e) hints at multiple generations/phases of silicification and suggests that the SA rinds may have acted as a template for very early silica precipitation (cf. Knoll, 1985). This further supports the argument for the rinds being an original feature of the micro-organism.

Deflected, underlying laminae

One mode of formation for the deflected underlying laminae beneath some SA microfossils could be compaction from deposition of overlying material during burial. However, this process would consistently produce bedding-parallel lens-shaped SAs and lens-shaped surrounding rinds, and symmetrically deflected upper and lower surrounding material, which is not the case for the specimens described here (Figure 1a). Instead, the fact that the shape of the microfossils is spherical (Figures 2d and 3d), or ellipsoidal perpendicular to bedding (Figure 1a; Figure 7a,b), and that only the material beneath the SAs is deflected, indicates that another process was responsible for the deformation of underlying laminae.

The deflected nature of the underlying laminae is compatible with local compaction from infalling planktonic SAs whose mucilaginous membranes (rinds) were at least partially silicified prior to having fallen into the sediment. Firstly, a planktonic origin for the SA microfossils is supported by the random arrangement of SA specimens within the chert-OM matrix (e.g. Figure S10), which

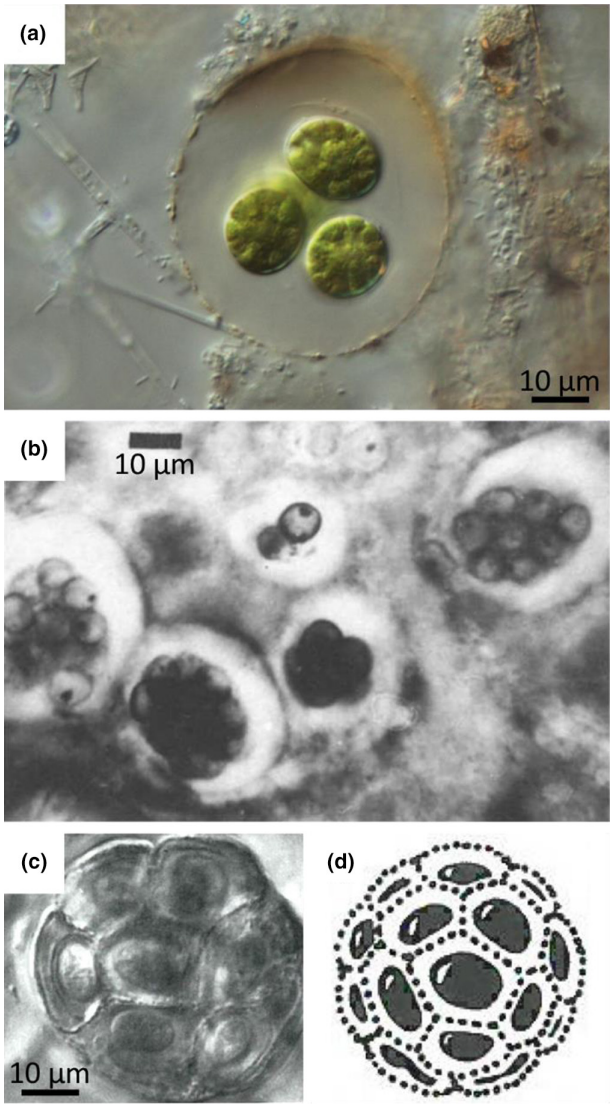

FIGURE 8 Examples of extracellular mucilage in an extant micro-organism, Asterococcus (a) and a fossilised micro-organism, *Eogloeocapsa avzyanica* (b). Note how the mucilage in both examples creates a clear, wide boundary around the cells that keeps the surrounding matrix material at bay. (c, d) 'Polyhedral packing morphology' in colonial micro-organisms: extant form Gloeothece (c) and sketch of extant form Gloeocapsa (d), showing tightly packed cells results in the cell envelope shape varying from spherical to pentagonal. Images from: (a) Matthews (2016); (b) Sergeev (1994); and (c, d) Golubic and Barghoorn (1977).

indicates they likely settled from a floating (planktonic) population (Moorman, 1974). In modern systems, planktonic micro-organisms come out of suspension in the water column and settle into OM-rich sediment on the seafloor when, for example, they encounter buoyancy changes, or density stratification in the water column (Guasto et al., 2012). The abundant, fluffy clots of OM present throughout these samples are also connotative of particulate OM having rained down on the sediment. In modern systems, such detritus is primarily derived from planktonic micro-organisms in overlying waters (Riley, 1971).

Secondly, early silicification of the rinds surrounding the SAs is supported by a recent study, which found that photosynthesis under Proterozoic-like conditions triggered silica precipitation in EPS due to localised changes in pH (Moore et al., 2021). This could provide a mechanism for the early mineralisation of the SA rind and could also explain the multiple phases of microquartz (i.e. the finer-grained microquartz in the rinds compared with the surrounding matrix) observed in some samples (see Section Clear outer rinds). In this scenario, early partial silicification of the SA micro-organisms and/or their surrounding mucilaginous membranes (rinds) may have caused them to drop out of suspension in the water column, fall down into very light, fluffy OM, and depress slightly the underlying bedded OM to create the locally deflected underlying laminae observed in the sections examined here. Variable silicification of the micro-organism and/or its surrounding rind may account for the observed differences in preserved rind morphology, including that only ~60% of specimens contained a distinct rind, and that some SAs have a thinned rind on their underside and a bulging, thicker rind on their topside (Figure S7c,d).

Jagged to wispy structures along irregular edge

The jagged to wispy wire-like structures on the outer edge of the main spheroidal body of the SA microfossils likely reflect a combination of partial preservation of compartment walls in the outermost parts of the SAs (in the case of the jagged edges) and possibly some local, super fine-scale mobilisation of OM around microquartz grain boundaries (in the case of the wispy edges).

However, it is also possible that taphonomic processes altered, but did not entirely destroy, an original morphological feature of the SA micro-organism. For example, younger, acritarch microfossils display processes and plexuses, which are recognised as original structures that emanated out from the body of these micro-organisms (Agic et al., 2015; Moczydłowska & Willman, 2009; Nagovitsin, 2009; Yin et al., 2021). Furthermore, taphonomic experiments on extant micro-organisms have shown that the morphology of flagella (superfine appendages that aid in colony movement) can be fossilised, albeit thicker silicified than when alive (Francis et al., 1978), raising the question of whether some of the fine kerogenous structures in the rinds of the SA microfossils could represent fossilised flagella. Additional work is needed to establish whether this could be the case.

Internal compartments and cell-like spheres

The characteristic internal compartments and their contained cell-like spheres could ostensibly have formed as diagenetic artefacts, whereby originally dispersed OM became distributed around mesocrystalline, or botryoidal, quartz crystals during diagenesis. However, the grainsize of the microquartz within the microfossils and their surrounding rinds is much finer than the size of either the compartments or the individual cell-like spheres (cf. Figures 5b, 6b and 5d,e,g and 6c,d), and botryoidal quartz (known to provide a template for OM resulting in the formation of vesicular shapes, see Coutant et al., 2022) has not been observed. This makes a diagenetic origin via OM mobilisation along quartz boundaries or templating on quartz crystals highly unlikely.

An alternative abiotic mode of formation of the honeycomb compartments and cell-like spheres could be OM mobilisation via diffusion in a silica gel prior to quartz mineralisation (e.g. Coutant et al., 2022). However, if either of these SA features had formed by diffusion of OM in a precursor silica gel, we would expect a number of additional components to be present in these samples that have not been observed, including: internal carbonaceous masses from which the 'cells' had formed; 'cell walls' made of diffuse, nanoparticulate OM that extends into the surrounding area; carbonaceous veins indicating mobilisation of OM throughout the sample; and evidence of OM diffusion gradients, such as Liesegang rings of OM, and/or multi-layered 'cell walls' (e.g. see figs. 1a, 1b, 8b of Coutant et al., 2022). A lack of such features in the material studied here thus indicates the honeycomb compartments and cell-like spheres are inconsistent with a diffusion origin.

Rather, the morphology of the honeycomb compartments and the cell-like spheres lends weight to a biogenic origin. The morphology of these features indicates they were affected by early taphonomic alteration, consistent with minor organic decomposition prior to silicification. For example, the gaps between the cell-like spheres and the surrounding compartment walls (e.g. Figure 6g) are consistent with decomposition experiments on extant micro-organisms in which water loss during decomposition causes cellular contents to shrink away from their surrounding sheaths (cf. fig. 1 of Knoll & Barghoorn, 1975). Sheaths are known to degrade more slowly than cells during initial decomposition prior to fossilisation (Bartley, 1996; Manning-Berg et al., 2022), which could explain why the honeycomb-like compartments have been observed in every SA specimen, but the cell-like spheres have not.

The difference in colour between the honeycomb compartments and the cell-like spheres may also provide insight into their origin. Each of the cell-like spheres consists of rich, amber brown-coloured OM that is distinct from the darker, granular OM of the honeycomb-like compartment walls (Figures 5 and 6). Darker-coloured OM is generally considered to indicate more degraded (i.e. more thermally altered/mature) material (Hayes et al., 1983; Knoll et al., 1988). However, given that both of these features were subject to the same temperature and diagenetic history, this colour variation may instead indicate that: (a) the honeycomb compartments represent structures that were more decomposed than the cell-like spheres prior to silicification; and/or (b) these two features were differently affected by thermal alteration during diagenesis, perhaps due to differences in the original composition of the OM (e.g. Igisu et al., 2009). An alternative explanation could be that the observed colour differences are reflective of density differences between these two features. This is supported by the CLSM data, in which the honeycomb compartments appear brighter (and therefore denser) than the cell-like spheres (Figure 6i,j). In any case, the difference in colour of the OM implies that the honeycomb compartments and the cell-like spheres could be the remains of original, distinct, cellular components.

In light of these observations and the very early silicification of the studied material (see Section Timing of silicification), the honeycomb-like compartments and cell-like spheres are interpreted to most likely represent the remains of cellular sheaths and shrunken cells, respectively. This is supported by the variability in shape of the SA compartments (i.e. sub-spherical to polygonal) being analogous to the 'polyhedral packing morphology' described from both extant and fossilised colonial forms (Figure 8c,d; Golubic & Barghoorn, 1977). This distinctive morphology occurs when a colony of cells is tightly packed together within an extracellular mucilage, causing the sheaths surrounding each individual cell to distort and exhibit a polyhedral shape (Golubic & Barghoorn, 1977). The shrinking of cells due to water loss during decomposition may have accentuated the polyhedral packing morphology in the SA microfossils (e.g. Figures 5d,e,g and 6j). As a result, the original diameter of the cell-like spheres is likely to have been larger than the ~11 μm average measured here.

The presence of multiple, smaller cell-like spheres within one compartment (Figure 6c,e) could be an appearance due to the cells having shrunk at different rates during initial decomposition prior to silicification (Golubic & Barghoorn, 1977). Alternatively, and considering the early silicification, we speculate whether these smaller cells could be evidence of asynchronous cellular division during reproduction, which is a trait documented in extant colonial micro-organisms (e.g. Menezes & Bicudo, 2008).

Variation in microfossil form

There is some variation in form between the individual SA specimens observed in this study. For example, the honeycomb-like compartments in some of the SAs contain amber brown cell-like spheres (Figures 5 and 6), whereas other specimens consist only of the dark-coloured, honeycomb-like network of compartments without any trace of enclosed cell-like spheres (e.g. Figures 1d and 3b). In still other examples, the honeycomb-like network of compartments is only preserved around the outer parts of the SAs, which appear to have a hollow core (Figures 3a; Figure S12e).

This variation in form among individual SAs could reflect variability in the extent of decomposition prior to silicification, whereby SAs with well-defined amber brown cell-like spheres could have been dead for a shorter period of time compared to the SAs with only the honeycomb-like network preserved. Taphonomic experiments on modern micro-organisms have shown that structurally compromised individuals decompose faster, resulting in a fossilised population with only a few very well-preserved specimens (Manning-Berg et al., 2022). This could explain the variation in form among specimens described here.

Alternatively, the variation in SA form could reflect natural variation in the original population, perhaps due to different cellular components being present at different stages of a life cycle. In view of this, perhaps the SAs with well-defined amber brown cell-like spheres were in a growth or reproductive state, whereas the SAs without the cell-like spheres were in a dormant, or decomposing state.

More likely, however, the variation in form is a combination of both natural variation in the original population and taphonomic alteration, reflecting the fact that any given population of micro-organisms contains a mixture of living, dormant, reproducing and/or decomposing organisms (Bartley, 1996). Another possibility, although considered unlikely, is that what is presented here as a single population of SAs may represent several different, but similar-looking, micro-organisms. Further work is required to establish whether this could be the case.

5.2.2 | Comparison to fossilised micro-organisms

The SA microfossils described here are morphologically distinct from microfossils currently known from the Archean and Paleoproterozoic. Microfossils from the Archean typically take the form of unicellular, filamentous or spindle-shaped (lenticular) structures (e.g. Czaja et al., 2016; Javaux et al., 2010; Klein et al., 1987; Knoll & Barghoorn, 1977; Sugitani et al., 2015; Walsh & Lowe, 1985; Figure S17a), and microfossils from the Paleoproterozoic, including the well-known Gunflint-type microbiota, generally consist of unicellular, filamentous and small radiating forms (e.g. Barghoorn & Tyler, 1965; Knoll & Barghoorn, 1976; Figure S17b). Broadly speaking, each of these morphologies can easily be differentiated from the SA morphology described here.

Having said this, there is some coarse similarity between the cell-like spheres *within* the SA microfossils and spheroidal structures recently described from the c. 3.4 Ga Strelley Pool Formation (SPF; Type 4 structures of Coutant et al., 2022), in that both consist of a sub-spherical morphology with an inner vesicle (cell) that is surrounded by an outer wall (sheath). However, there are prominent differences in overall colony/cluster appearance and configuration between these two examples. Specifically, the cell-like spheres of the SA microfossils are consistently aggregated into an overall spherical, colonial morphology of regular size and shape, with tens of aggregates observed across multiple thin sections (Figures 1–3), whereas the spheroidal structures of the SPF were observed within only one cluster, and this had a contorted, non-uniform overall shape (Figure S17c, left side; Coutant et al., 2022). Moreover, the SPF spheroidal structures are loosely arranged and sit among a thick concentration of nanoparticulate OM that is distributed both in and around the structures (Figure S17c, middle and right side), which may suggest cluster formation via adhesion of individual cells rather than cell division (e.g. Xiao et al., 2017). In contrast, the cells in the SA microfossils described here are bound by a continuous honeycomb network (polyhedrally packed sheaths; Figures 1d and 6j) within a silicified rind (mucilaginous membrane; Figure 6h), signifying that the SA microfossils are discrete, structured colonies.

The large size of the SA microfossils and their overall morphology, comprising individual, multicellular colonies of consistent size and shape, indicate a different mode of organisation not seen among known microfossils of Archean and Paleoproterozoic age

(Figure S17). The appearance of this discrete, new multicellular morphology coincident with the rise in atmospheric oxygen suggests a change in lifestyle and a step-up in morphological organisation.

A thorough literature search of the younger fossil record has uncovered four microfossils that somewhat resemble the SAs in overall morphology, but that fail to represent a directly compatible counterpart for the SA microfossils (Figure 9). The first of these is a coccoidal, planktonic microfossil from deep water, siliceous black shales of the Neoproterozoic Hector Formation in Canada (Moorman, 1974). This microfossil is part of a population of microfossils interpreted to represent a single species, *Sphaerocongregus variabilis*, with a range of growth forms (see fig. 3 of Moorman, 1974). One of the forms broadly resembles the SA microfossils of the TCG in overall morphology (Figure 9a). However, there are some important distinctions: (1) we have not observed variation in SA morphology that would indicate a growth cycle such as that documented in Moorman (1974) (e.g. specimens ranging from small individual spherical cells, to a colony with only a couple/few cells, to a colony with multiple/many cells); (2) there is no evidence in the SA microfossils of reproduction by endosporulation or binary fission of unicellular forms as documented for the Hector Formation microfossils; (3) the SAs contain a wide, clear rind, which is not described for the Hector Formation microfossils; (4) there is a large difference in colony diameter: ~5–20 μm for the Hector Formation microfossils compared to ~52 to 162 μm for the SAs; and (5) the cell size is vastly different: ≤2 μm diameter in the Hector Formation microfossils, versus ~15 μm (av.) diameter compartments in the SAs (cf. Figure 9a$_1$ and 9e$_1$, f$_1$).

The second example of a microfossil that broadly resembles the SAs described here is *Eogloeocapsa avzyanica* Sergeev, documented from the Late Mesoproterozoic Kataskin Member of the Avzyan Formation, Russia (Sergeev, 1994). This microfossil consists of small clusters of cells, ~8–23 μm in diameter, surrounded by a wide, clear envelope that increases the overall diameter to up to ~60 μm (Figure 9b). Two generations of daughter colonies were commonly observed within the outer envelope of *E. avzyanica* (see fig. 5a,b of Sergeev, 1994). Although there is some similarity between these microfossils and the SA microfossils described here in the form of clustered cells surrounded by an outer rind, the primary distinctions are: (1) the common occurrence in the younger microfossils of multiple distinct colonies within a single envelope, which was not observed here; and (2) the considerable difference in the size of both the colony and the contained cells (cf. Figure 9b$_1$ and 9e$_1$, f$_1$).

The third example of a broadly similar microfossil morphology is an acritarch, *Timofeevia*, from a Cambrian deposit in Nova Scotia, Canada (Figure 9c; Palacios et al., 2012). The presence of honeycomb-like scaffolding and processes in *Timofeevia* could be comparable to the SA honeycomb-like framework of compartments and the wispy, wire-like structures, respectively. However, there are key differences between these two microfossils: the acritarch has numerous well-pronounced processes, appears as a hollow sac that lacks any internal structure, does not have a wide, clear rind, and is much smaller (only up to ~30 μm diameter; cf. Figure 9c$_1$ and e$_1$, f$_1$).

The fourth example of a broadly comparable microfossil morphology is the Ediacaran microfossil, *Megasphaera minuscula*, described by Anderson et al. (2019) from a Mongolian phosphorite deposit. *Megasphaera minuscula* consists of a large, spheroidal vesicle up to ~325 μm diameter, with a smooth, unornamented wall that encloses numerous internal cellular structures (Figure 9d). Variable preservation makes both the size range and the number of internal structures particularly difficult to assess, but these structures have been estimated to range from 3 to 26 μm diameter and number between 20 and 106 per vesicle (Anderson et al., 2019).

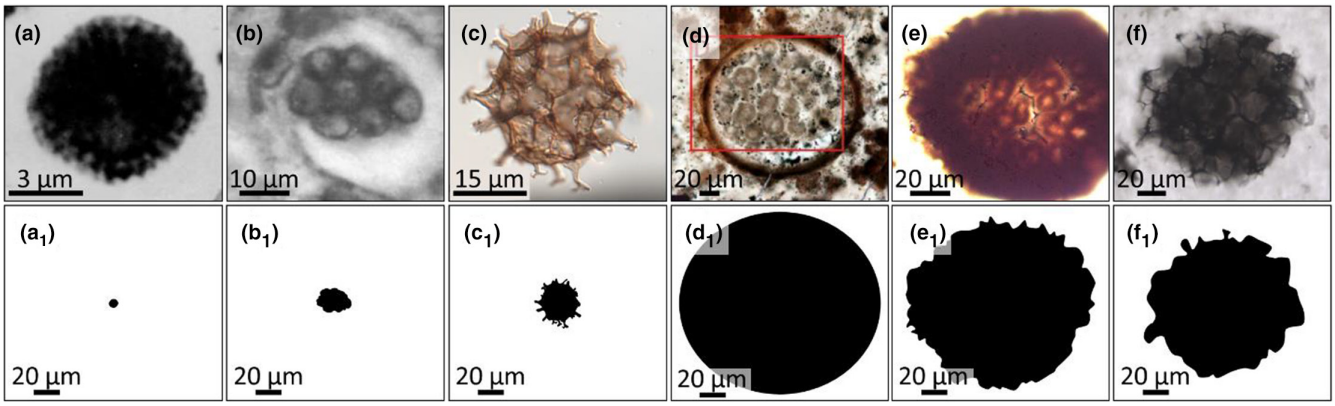

FIGURE 9 Comparison between the Turee Creek Group SA microfossils and younger fossilised micro-organisms that contain some broadly similar morphological features. (a) Pleurocapsa-like microfossil from the Neoproterozoic Hector Formation (image from Moorman, 1974). (b) Chroococcoid cyanobacterial microfossil from the Late Mesoproterozoic Avzyan Formation (image from Sergeev, 1994). (c) An acritarch, Timofeevia, from the Cambrian McMullin Formation (image from Palacios et al., 2012). (d) *Megasphaera minuscula* microfossil preserved in phosphorite from the Ediacaran upper Khesen Formation (red box is from original image used in Anderson et al., 2019). (e, f) The large spherical aggregate microfossils studied here. (a1–f1) Schematic drawings of the microfossils in parts (a–f), resized to be shown at the same scale as one another to highlight the colossal differences in size. Note that the specimen in (e) is overexposed to show its internal structure more clearly, but that this removes detail of the outside of the SA microfossil, meaning the overall size of this specimen is larger than depicted in (e). For the comparative size diagram in (e1), the full size of this specimen (see Figure 5a) has been used.

Of the four examples spotlighted above, *M. minuscula* is most similar to the SA microfossils when compared across all morphological attributes (Figure 9). Similarities include: an overall spherical morphology; relatively comparable size (mean *M. minuscula* diameter = 136 μm, mean SA diameter = 97 μm); and the presence of multiple internal cellular structures whose exact number and size range are difficult to estimate due to their tightly clustered nature and indifferent preservation (Anderson et al., 2019).

Nevertheless, there are still key variations between the Ediacaran *M. minuscula* microfossil and the Paleoproterozoic SA microfossils. In addition to the different preservation medium (i.e. phosphorite versus chert), the *M. minuscula* microfossil differs from the SA microfossils in that it: constitutes a single vesicle containing cells, as opposed to an aggregate of cells held together by a mucilaginous membrane; is characterised by a smooth, continuous, outer wall that lacks processes or ornamentation; has a broader size range of 76–325 μm diameter (compared to the SAs range of 52–162 μm diameter); lacks a honeycomb-like framework encapsulating the internal cells; and does not have a rind (evidence of a mucilaginous membrane; cf. Figure 9d_1 and e_1, f_1).

5.2.3 | Comparison to extant micro-organisms

Due to a lack of compatible fossil counterparts for the SAs, we present a comparison with extant colonial micro-organisms as a way to glean insights into possible classification and morphological form and function.

Many extant bacterial micro-organisms have a unicellular morphology, but bacteria that specifically form aggregates (colonies) with multiple cells are known within the non-filamentous Cyanobacteria (Margulis & Chapman, 2009), with common colony-forming genera including *Chroococcus*, *Eucapsis*, *Chroococcidiopsis*, *Microcystis*, *Asterocapsa* and *Coelosphaerium* (Figure S18). These bacterial colonies form via cell division (e.g. binary fission, where the produced cells stay attached) and/or cell adhesion (where cells group and stick together), which commonly results in clumped, arbitrarily distributed, masses of cells (Garcia-Pichel, 2009; Xiao et al., 2017; Figure S18d,f). Cyanobacterial colonies are variable in both shape and size, forming regular, irregular or spherical clusters that range from <10 μm wide (a few cells) to >1000 μm wide (hundreds or more cells) (Figure S18; Xiao et al., 2018). Generally, individual cells within a cyanobacterial colony are small (~2–6 μm diameter), with either a hemispherical, subspherical, spherical, or ovoid form (Komarek & Johansen, 2015). It is common for colonies and, in some cases, individual cells within a colony, to be enveloped by clear, mucilaginous sheaths (Whitton, 2011).

The SA microfossils partially resemble some coccoidal, colony-forming cyanobacteria (e.g. *Pleurocapsa* spp., *Chroococcopsis* spp.) in terms of having a spherical cell shape and the presence of colonial and/or cellular mucilage (Table 1). However, these features are not particularly diagnostic, as they are common to a wide range of micro-organisms from across the tree of life (John et al., 2011).

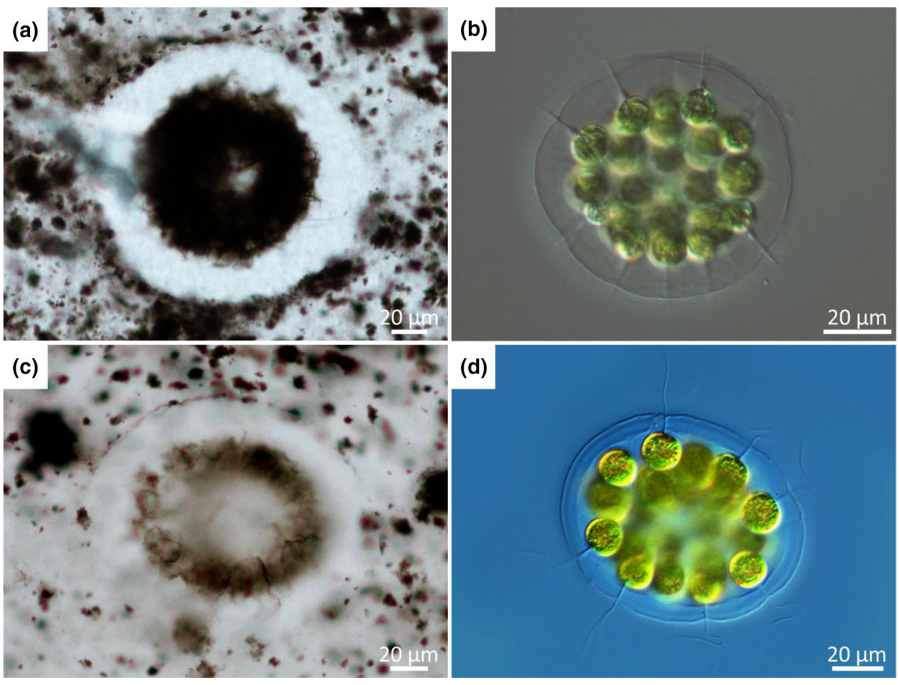

FIGURE 10 Direct comparison of Turee Creek Group SA microfossils (a, c) and extant, Volvocacean coenobial algae (Eudorina; b, d). Note similarities in symmetrical shape, structure and overall size. Spherical (a) and ellipsoidal (c) microfossils with wide, kerogen-free rinds; PPL. Compare with spherical (b) and ellipsoidal (d) coenobia that are surrounded by thick, clear, extracellular mucilage. Also note the thin, wire-like structures and apparent hollow centre of the microfossil in part (c) (and the hint of a hollow centre within the specimen in part a) and compare with the flagella and hollow centre of the coenobia in parts (b) and (d). Image credit: (b) Matthews (2016) and (d) Antonio Guillén.

TABLE 1 Summary of morphological analysis comparing the TCG large SA microfossils to extant colonial bacteria and extant coenobial algae (see also Figures S18 and S19).

		TCG large spherical aggregate microfossils	Extant colonial bacteria (phylum: Cyanobacteria)	Extant coenobial algae (spherical colonies in the family: Volvocaceae)
Colony	Shape	Generally spherical, some slightly ellipsoidal	Variable: regular packets of cells in neat, planar (or cubic) arrangements (e.g. *Chroococcus*, *Eucapsis*)[1,2]; broadly spherical, but slightly irregular (e.g. *Coelosphaerium*)[1]; initially spherical, but morphs into an irregular, asymmetric mass with continued growth (e.g. *Microcystis*)[3]	Highly ordered and symmetrical: spherical, ellipsoidal or ovate (egg-shaped)[6,7]
	Size	Ranges from ~52 to 162 μm diameter (majority of observed specimens >90 μm), with >20 cell-like spheres per microfossil	Ranges from <10 μm diameter (a few cells) to >1000 μm diameter (hundreds or more cells)[1–3]	Ranges from ~50 to 200 μm diameter in mature coenobia, which contain 16 or 32 cells (both colony size and number of cells is dependent on genera)[6–11]
	Mucilage	Surrounded by a ~20 to 30 μm wide rind interpreted as corresponding to extracellular mucilaginous membrane	Colonies surrounded by mucilage[1,2]	Each coenobium is contained within a clear, smooth, extracellular mucilaginous membrane[6–8,12]
	Distribution	Preserved as individual, solitary forms	Clumped, patchily distributed, and/or arbitrarily arranged masses	Distinct, individual coenobium
Cells within colony	Shape	Cell-like spheres are spherical to sub-spherical	Hemispherical, spherical, ovoid, or heart-shaped (depending on genera)[1,2]	Spherical, ovoid or keystone-shaped (depending on genera)[10,13]
	Size	Cell-like spheres ~11 μm diameter, honeycomb compartments ~15 μm diameter	Most are ~2–6 μm diameter (although *Chroococcus* cells can be larger)[1,2]	Most are >10 μm diameter, but can range from 5 to 25 μm depending on genera and age[6,11]
	Mucilage	Honeycomb-like compartments, interpreted as remains of cellular sheaths, are spherical, sub-spherical, or polygonal in shape	In some examples, mucilaginous sheaths surround individual cells, in addition to the colony mucilage (e.g. *Gloeocapsa*)[1,2]	Cells are contained within individual gelatinous sheaths, which appear spherical or hexagonal in surface view[7,9,11,14]
	Distribution	Cell-like spheres are densely packed, with surrounding sheaths forming a honeycomb-like framework	Cells are commonly irregularly arranged within the colony, but some genera have cells distributed in 'packets' (e.g. planar or cubic arrangements)	Cells are tightly-packed, with surrounding gelatinous sheaths forming a tessellated pattern; in some coenobia, cells are arranged around the periphery, forming a hollow sphere[10,13]
Other	Motility	Thin wire-like structures, <1 μm wide and ~5–20 μm long, could be remains of flagella(?)	Although some colonies may act cooperatively, for example exhibiting phototaxis, or 'social motility'[4], they are generally not considered to be motile; individual cells do not contain flagella[5]	Coenobia are motile; each cell contains 2 whip-like flagella that enable colony movement within the water column[13]; flagella length estimated at ~15–35 μm[13,15]
	Reproduction	Multiple cell-like spheres clustered within single compartments could be evidence of asynchronous cell division in asexual reproduction of colony	Individual cells undergo binary fission[5]	Coenobia reproduce through asexual or sexual means[7,10]; asexual reproduction may by synchronous or asynchronous[9] (see Figure 11f)
	Lifestyle; habitat	Likely planktonic; could have lived in lagoonal or more open-water setting	Mixed[1]	Planktonic[16]; predominantly freshwater habitat, but have been found in oligohaline lagoonal settings[9,17]

Note: Morphological similarity with the SA microfossils is indicated by the light grey and dissimilarity by the dark grey. Numbered references: 1: Komarek and Johansen (2015); 2: Whitton (2011); 3: Xiao et al. (2018); 4: Muñoz-Dorado et al., (2016); 5: Garcia-Pichel (2009); 6: Pentecost (2011); 7: Goldstein (1964); 8: Matthews (2016); 9: Menezes and Bicudo (2008); 10: Nozaki et al. (2014); 11: Yamada et al. (2008); 12: Herron and Nedelcu (2015); 13: Nakada and Nozaki (2015); 14: Prescott (1955); 15: John et al. (2011); 16: Reynolds (1984); and 17: Onuoha et al. (2010).

More importantly, there are multiple differences between the SA microfossils and extant cyanobacterial colonies (Table 1). Specifically, the size, shape and distribution of cyanobacterial colonies varies widely, whereas the SA microfossils are comparably limited in both size (with most specimens between ~83 and 110 μm diameter; Figure S6b) and shape (consistently spherical-ellipsoidal), resulting in distinct, individual specimens. Moreover, cyanobacterial cell size (~2–6 μm diameter; Whitton, 2011) is much smaller than the cell-like spheres and honeycomb-like compartments in the SA microfossils (av. ~11 and ~15 μm diameter, respectively); this is especially so considering these SA features likely shrunk prior to silicification (e.g. Knoll & Barghoorn, 1975). Combined, these differences in colony size, shape and distribution, as well as individual cell size and distribution, indicate the SA microfossils are morphologically dissimilar to known extant cyanobacterial colonies.

Other extant, colony-forming micro-organisms include coenobial algae. Compared to bacterial colonies, coenobial algae form distinct, individual colonies consisting of a definite number of cells that are generally much larger than bacterial cells and are consistently arranged in an organised, regular structure (Pentecost, 2011). For example, planktonic green algae within the family Volvocaceae, such as *Pandorina*, *Eudorina*, *Yamagishiella* and *Colemanosphaera*, form ordered symmetrical colonies that are consistently spherical, or slightly ellipsoidal, in shape (Figure S19; Nozaki et al., 2014; Nakada & Nozaki, 2015). Depending on the genera and the age of the colony, these coenobial algae contain 16 or 32 closely packed cells that are generally between 10 and 25 μm in diameter (Yamada et al., 2008).

Interestingly, each of the morphological features described in the SAs here can be matched to an apparently analogous morphological feature within extant Volvocacean coenobial algae (Table 1). Both the SAs and the extant Volvocacean coenobial algae have a consistently ordered, symmetrical, spherical to ellipsoidal shape (Figure 10); the size range of the SAs (~52–162 μm diameter) is within the range known for the extant coenobial algae (~50–200 μm, where size is dependent on stage in life cycle; Matthews, 2016); and the kerogenous, spherical rind that envelops the SAs is analogous to the extracellular mucilaginous membrane that encloses the coenobial algae (cf. Figure 10a,c and 10b,d). The distribution of individual specimens is also similar, with the SAs preserved as singular, solitary forms and the Volvocacean algae as distinct, individual coenobia (cf. Figure 2 and Figure S19).

Importantly, the shape, size and distribution of the individual cells within the SAs also resembles those of the Volvocacean coenobial algae (Figure 11). Specifically, the cell-like structures that comprise the SAs are spherical and ~11 μm in average diameter (note, this size is likely underestimated due to taphonomic cell shrinkage; see Section Internal compartments & cell-like spheres). This shape and size are analogous to the coenobial algae cells, which are spherical to ovoid and are typically >10 μm diameter, but can be up to 25 μm diameter depending on genera and age (Pentecost, 2011; Yamada et al., 2008; Table 1). Each SA microfossil contains >20 cell-like spheres, with each cell surrounded by a sub-spherical to hexagonal compartment. These features are comparable to the Volvocacean coenobial algae, which consist of a distinct number of cells (usually 16 or 32, depending on genera) that are individually surrounded by spherical-polygonal gelatinous sheaths (Menezes & Bicudo, 2008; Prescott, 1955). In particular, the tightly packed nature of the extant algal cellular sheaths makes a tessellated pattern that exactly resembles the honeycomb-like network of compartments preserved in the SAs (Figure 11a–d). There are also similarities in the distribution of cells: those in most specimens of both the SA microfossils and extant coenobial algae are densely packed (Figure 11), whereas in some specimens, cells are arranged around the periphery leaving the centre of the specimen hollow (Figure 10c,d).

In the coenobial algae cells, there are clear central spots known as pyrenoids that are involved in the accumulation and fixation of carbon (Figure S19; Giordano et al., 2005). Although pyrenoids themselves are unlikely to be fossilised, recent taphonomic experiments on unicellular and multicellular algae have shown that the presence of pyrenoids can be inferred by distinctive 'holes' left behind after the rest of the cell contents have decayed (Carlisle et al., 2021). This process could explain the clear central domains observed in some of the SA cells (e.g. Figure 11a,c,e), although these domains are mostly centred in the middle of the cell-like spheres, rather than irregularly positioned relative to the cell wall, as in the modern taphonomic experiments of Carlisle et al. (2021). Having said this, the pyrenoids visible in Volvocacean coenobia (e.g. Figure S19b–d) appear mostly centred relative to the cell walls. It is also possible that the clear central spots in the SA microfossils could represent a different cellular structure, such as a vacuole, or that the spots could be an artefact of cellular degradation and/or subsequent mineralisation. Additional work on Volvocacean coenobia and other modern colonial micro-organisms is required to ascertain the types of degradation and taphonomic alteration patterns of cells and cellular structures.

The same can be said for the taphonomic degradation of flagella in coenobial Volcocaceae. The thin, wire-like structures that extend outwards from the SA microfossils into the clear rind correspond closely, in terms of size, shape and location, to flagella in extant coenobial algae (Figure 10c,d). What is not clear, however, is whether the distribution is also analogous (i.e. two wire-like structures per cell-like sphere, reflecting two flagella per cell in the Volvocacean algae). With the data and petrographic observations presented here, a taphonomic origin for the SA wire-like structures cannot be ruled out and further work in this area is warranted.

Other notable similarities between the SAs and extant Volvocacean coenobial algae include: multiple, smaller cell-like spheres clustered within single compartments in the SAs that resemble asynchronous daughter colony formation in the extant coenobial algae (Figure 11e,f; Menezes & Bicudo, 2008); and a planktonic lifestyle for both microfossil (see Section Deflected, underlying laminae) and coenobial algae (Reynolds, 1984).

It is possible that the type of habitat may also be analogous. Although a specific habitat for the SA microfossils is difficult to ascertain, as a planktonic lifestyle does not constrain the location

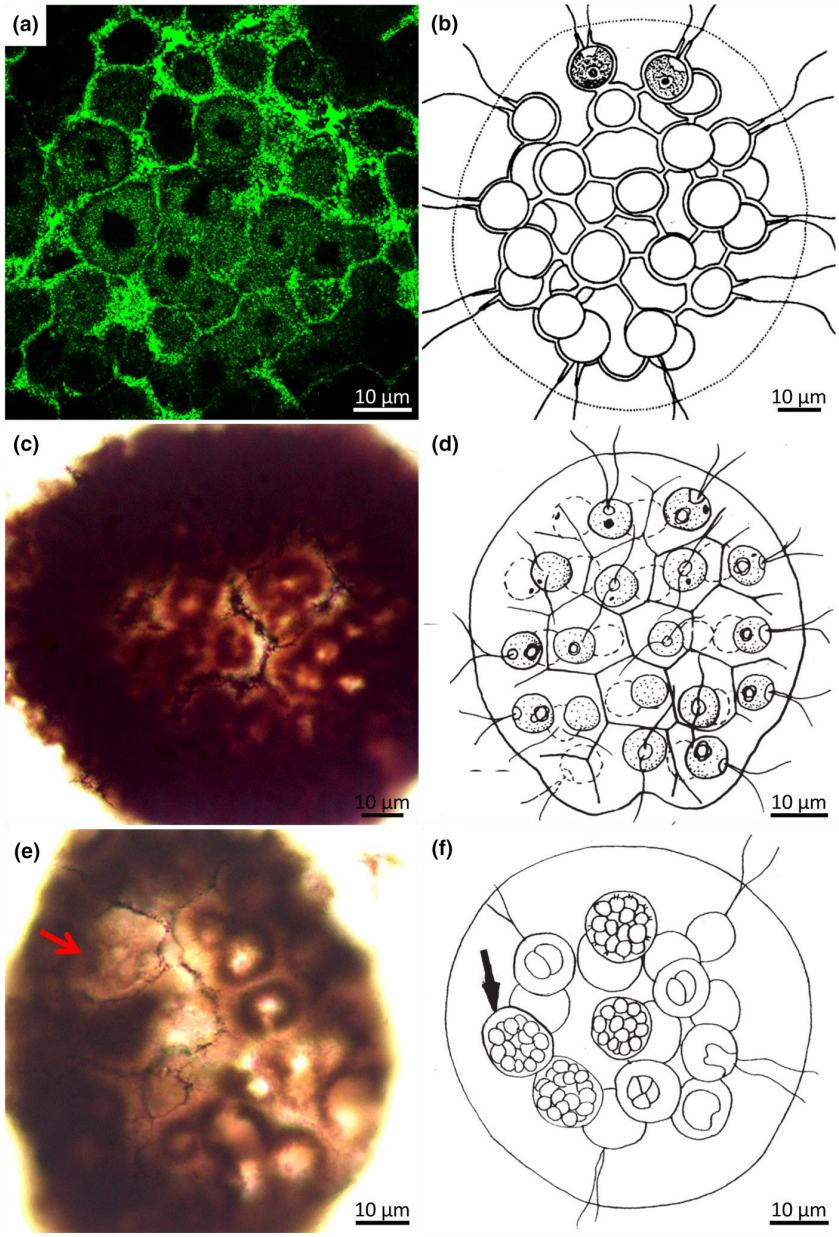

FIGURE 11 Direct comparison of Turee Creek Group SA microfossils (a, c, e) with illustrations of extant, Volvocacean coenobial algae (Eudorina; b, d, f). Note overall similarities in size, shape and structure. (a) CLSM image of a SA microfossil highlighting the interconnected nature of the spherical, honeycomb-like compartments. Compare with sketch of Eudorina coenobium (b), where spherical cells are individually surrounded by spherical sheaths that are interconnected with neighbouring sheaths. (c) Large (~137 μm diameter) SA microfossil with pentagonal to hexagonal compartments that enclose tightly packed, cell-like spheres; PPL. Note the clear, central domains within the middle of each sphere (also visible in parts a and e). Compare with sketch of Eudorina coenobium (d), where tightly packed cells (containing round, central pyrenoids) are individually surrounded by slightly irregular, hexagonal sheaths. (e) SA specimen that contains multiple, smaller cell-like spheres within one compartment (red arrow). Compare with sketch of Eudorina coenobium (f), showing asynchronous daughter colony formation during asexual reproduction. Note the similarities in size between the small cell-like spheres in the microfossil (red arrow in part e) and the daughter cells in the extant coenobium (black arrow in part f). Sketch credit: (a) Prescott (1955) and (d, f) Menezes and Bicudo (2008). Scale in part (b) is estimated from reported diameter (89 μm) of sketched colony.

within the depositional system from which the SAs may have come, they may have inhabited either the lagoonal or more open-water portion of the TCG microbialite reef complex. In comparison, extant Volvocacean algae have primarily been documented as living in freshwater habitats, although there are rare instances reported from oligohaline (brackish) settings, such as lagoons (e.g. *Gonium formosum*; Menezes & Bicudo, 2008, *Eudorina elegans* Onuoha et al., 2010).

Overall, the ensemble of corresponding features illustrates a distinct similarity between the SAs and extant coenobial algae from the Volvocaceae family (Table 1). This similarity should not be interpreted to indicate that the SAs *are* ancient Volvocacean algae,

necessarily, as microfossils cannot be classified based on morphology alone (Schopf, 1993). Rather, this similarity (Table 1) indicates that the SA microfossils display a resemblance to the type of cellular organisation exhibited by modern algal coenobia, reinforcing the relative complexity of the SA microfossil form.

This comparative morphological analysis with extant coenobial micro-organisms affords important insight into the form and possible function of observed SA morphological characteristics and provides a valuable starting point for discussion around aspects such as the possible reproductive, lifestyle and habitat traits of these microfossils.

5.2.4 | In situ carbon isotope interpretation

The range of $\delta^{13}C$ data collected here from the SA microfossils (−32.2‰ to −24.6‰) differs from the matrix OM (−37.2‰ to −29.1‰; Figure 7). However, with weighted means only 1.4‰ apart, and within error of one another, this difference is difficult to interpret. Even so, such heterogeneity in carbon isotopic composition within a single sample is thought to be reflective of primary differences in microbial metabolism and/or variation in the composition of biologically available carbon within the localised environment (House et al., 2000).

The likely metabolic pathway utilised by a micro-organism to fix carbon can be inferred from the extent of isotopic fractionation ($\Delta^{13}C$; see Supplementary Discussion). Using a calculated estimate of the carbon isotopic composition of dissolved inorganic carbon (DIC ≈ +1.9‰), representing the starting substrate for carbon fixation, the total fractionation ($\Delta^{13}C$) recorded by our data is >15‰ (Figure S20; Table S6). This rules out four of the six currently known reaction pathways used by autotrophic micro-organisms to fix carbon (Hugler & Sievert, 2011), leaving the Calvin cycle (i.e. RuBisCO-driven photosynthesis) and the acetyl-CoA pathway as possible analogues to explain the SA isotopic values. Although both pathways result in similar fractionation (Preuss et al., 1989), making it difficult to differentiate between the two based on carbon isotope data alone, they can be distinguished given depositional and contextual evidence. Specifically, the acetyl-CoA pathway contains oxygen-sensitive enzymes and is only active in anoxic, highly reducing environments (Berg et al., 2010; Hugler & Sievert, 2011). Given that petrographic and textural observations support a planktonic lifestyle for the SAs (see Section Deflected, underlying laminae) and that the shallow waters of the TCG were, at least locally, highly oxygenated (Soares et al., 2019), our data are most consistent with fractionation produced during RuBisCO-driven carbon fixation via the Calvin cycle.

Other research investigating the in situ carbon isotopic composition of ancient microfossils has reportedly been able to discriminate between the products of prokaryotic and eukaryotic RuBisCO-driven photosynthesis (Williford et al., 2013). In this light, the carbon isotopic composition of the SAs (w. mean $\delta^{13}C$ −30.4 ± 2.3‰) appears to be consistent with fractionation produced from both extant and fossil eukaryotes ($\delta^{13}C \approx -29‰$ and $\delta^{13}C \approx -30‰$, respectively; Roeske & O'Leary, 1984; Williford et al., 2013) and inconsistent with data from cyanobacterial RuBisCO-driven photosynthesis, which produces much heavier values ($\delta^{13}C \approx -23‰$; Williford et al., 2013).

6 | CONCLUSION

Presented here are new petrographic, morphologic and in situ carbon isotopic data on a novel type of large SA microfossil from the c. 2.4 Ga TCG in Western Australia. Morphological and contextual observations were used to characterise this microfossil, and comparative morphological analyses with fossil and extant micro-organisms provided insight into the SA microfossil form and the possible function of specific SA microfossil characteristics.

Comparative analysis with microfossils from before the GOE revealed the large SA microfossil morphology represents a step-up in organisation, with a more complex cellular arrangement compared to microfossils currently known from the Archean. Comparative analysis with younger, Proterozoic microfossils found no compatible morphological counterpart for the SA microfossils, rendering this distinctive morphology currently unknown from the geological record.

Comparative analysis with extant micro-organisms revealed a morphological dissimilarity between the SA microfossils and modern coccoidal bacteria. In contrast, this analysis also uncovered a marked resemblance between the morphology of the SA microfossils and extant algal colonies, with explicit similarities in: overall colony shape, size and distribution; individual cell shape, size and distribution; the presence of mucilaginous membranes around both cell and colony; and evidence for motility, reproduction and habitat. This suite of analogous features indicates the SA microfossil has an organised morphology akin to extant eukaryotic algae. In situ carbon isotopic data support this finding, with fractionation that is consistent with that reported from both extant and fossil eukaryotes.

These results from both fossil and extant comparative morphological analyses prompt the question of whether the large SA microfossils may represent an early eukaryotic micro-organism. If this were the case, it would extend the record of eukaryotic microfossils by ~750 million years, from the currently accepted oldest eukaryotes at ~1.65 Ga (Miao et al., 2019). This long time-gap could, in part, reflect the exceptional level of preservation in the TCG microbialite reef complex studied here, but also, the preservational bias of the geological record, which lacks well-preserved microfossils throughout the early Paleoproterozoic: there simply are no other well-preserved microbial reefs known from the GOE anywhere in the world. Indeed, studies of both eukaryal sterol biosynthesis and molecular clocks estimate the rise of eukaryotes in the Paleoproterozoic (Betts et al., 2018; Gold et al., 2017; Parfrey et al., 2011),

providing independent support for an earlier appearance of eukaryotes than the current fossil record suggests.

Nevertheless, we recognise there are challenges in ascribing affinities to ancient microfossils, especially in the absence of definitive biomolecules (which are unlikely to be preserved here given the thermal maturity of these rocks; Fadel et al., 2017; Williford et al., 2011). The SA microfossils join the growing collection of Archean and Paleoproterozoic fossils regarded as proto-eukaryotes—those whose affinity is unable to be conclusively determined, but whose morphology connotates complexity in terms of size (Czaja et al., 2016; El Albani et al., 2010, 2019; Han & Runnegar, 1992; Javaux et al., 2010; Sugitani et al., 2010) and/or organisational structure (Bengtson et al., 2017; González-Flores et al., 2022; Sasaki et al., 2022).

Irrespective of exact classification, the remarkable preservation in the cherts studied here has enabled insight into the morphology and possible habitat, reproduction and metabolism of the large SA microfossils. In particular, the relatively large size of the SA microfossils and their contained cells, combined with their overall morphology consisting of individual, multicellular colonies of consistent size and shape, distinguish them from other microfossils preserved in Archean and Paleoproterozoic rocks. This study reveals a step-up in morphological organisation coinciding with the GOE, hinting at the co-evolution of life and environment at this time.

ACKNOWLEDGMENTS

We acknowledge the Puutu Kunti Kurrama and Pinikura peoples as the custodians of the land on which we conducted field work for this study. Thank you to M. & D. Avery for field access; J. Jesse, B. Nomchong, and G. Soares for field assistance; J. Wilde, J. Duggan and M. Bebbington for assistance with sample preparation; and A. Czaja for generously providing use of and assistance with the CLSM. Thank you to S. Porter, M. Gehringer, A. Manning-Berg, B. Burns and B. Teece, who provided feedback on earlier versions of this manuscript, and to R. Buick for editorial handling. EVB acknowledges support from the Australian Centre for Astrobiology; the UNSW Paleontology, Geobiology and Earth Archives (PANGEA) Research Centre; an Australian Government Research Training Program Scholarship; and an appointment to the NASA Postdoctoral Program at Pennsylvania State University and the Laboratory for Agnostic Biosignatures, administered by Oak Ridge Associated Universities under contract with NASA. EVB and MVK acknowledge funding support from the Australian Research Council Centre of Excellence for Core to Crust Fluid Systems (CCFS: CE1101017). EVB and CHH acknowledge support from NASA Astrobiology NfoLD grant #80NSSC18K1140, and CHH acknowledges support from NSF grant #EF-1724099. The UCLA ion microprobe facility is partially supported by a grant from the NSF Instrumentation and Facilities program.

CONFLICT OF INTEREST STATEMENT

The authors declare that they have no conflict of interest.

DATA AVAILABILITY STATEMENT

All data generated or analysed during this study are included in this published article and its supplementary information file. Correspondence and requests for material should be addressed to EVB (evbarlow@gmail.com).

ORCID

Erica V. Barlow https://orcid.org/0000-0001-6234-1343

REFERENCES

Agic, H., Moczydlowska, M., & Yin, L.-M. (2015). Affinity, life cycle, and intracellular complexity of organic-walled microfossils from the Mesoproterozoic of Shanxi, China. *Journal of Paleontology*, *89*, 28–50.

Anderson, R. P., McMahon, S., Macdonald, F. A., Jones, D. S., & Briggs, D. E. (2019). Palaeobiology of latest Ediacaran phosphorites from the upper Khesen Formation, Khuvsgul Group, northern Mongolia. *Journal of Systematic Palaeontology*, *17*(6), 501–532.

Barghoorn, E. S., & Tyler, S. A. (1965). Microorganisms from the Gunflint chert. *Science*, *147*, 563–575.

Barley, M., Pickard, A., & Sylvester, P. (1997). Emplacement of a large igneous province as a possible cause of banded iron formation 2.45 billion years ago. *Nature*, *385*, 55–58.

Barlow, E., Van Kranendonk, M. J., Yamaguchi, K. E., Ikehara, M., & Lepland, A. (2016). Lithostratigraphic analysis of a new stromatolite-thrombolite reef from across the rise of atmospheric oxygen in the Paleoproterozoic Turee Creek Group, Western Australia. *Geobiology*, *14*, 317–343.

Barlow, E. V. (2019). Diversification of early life: Microfossils of the c. 2.45–2.21 Ga Turee Creek Group, Western Australia. PhD thesis, University of New South Wales, Sydney, 273 p.

Barlow, E. V., & Van Kranendonk, M. J. (2018). Snapshot of an early Paleoproterozoic ecosystem: Two diverse microfossil communities from the Turee Creek Group, Western Australia. *Geobiology*, *16*, 449–475.

Bartley, J. K. (1996). Actualistic taphonomy of cyanobacteria: Implications for the Precambrian fossil record. *Palaios*, *11*, 571–586.

Bekker, A., Krapež, B., & Karhu, J. A. (2020). Correlation of the stratigraphic cover of the Pilbara and Kaapvaal cratons recording the lead up to Paleoproterozoic icehouse and the GOE. *Earth-Science Reviews*, *211*, 103389.

Bengtson, S., Rasmussen, B., Ivarsson, M., Muhling, J., Broman, C., Marone, F., Stampanoni, M., & Bekker, A. (2017). Fungus-like mycelial fossils in 2.4-billion-year-old vesicular basalt. *Nature Ecology & Evolution*, *1*(6), 1–6.

Berg, I. A., Kockelkorn, D., Ramos-Vera, W. H., Say, R. F., Zarzycki, J., Hügler, M., Alber, B. E., & Fuchs, G. (2010). Autotrophic carbon fixation in archaea. *Nature Reviews Microbiology*, *8*, 447–460.

Betts, H. C., Puttick, M. N., Clark, J. W., Williams, T. A., Donoghue, P. C., & Pisani, D. (2018). Integrated genomic and fossil evidence illuminates life's early evolution and eukaryote origin. *Nature Ecology & Evolution*, *2*, 1556–1562.

Brasier, M. D., Green, O. R., & McLoughlin, N. (2004). Characterization and critical testing of potential microfossils from the early Earth: The Apex "microfossil debate" and its lessons for Mars sample return. *International Journal of Astrobiology*, *3*, 139–150.

Caquineau, T., Paquette, J. L., & Philippot, P. (2018). U-Pb detrital zircon geochronology of the Turee Creek Group, Hamersley Basin, Western Australia: Timing and correlation of the Paleoproterozoic glaciations. *Precambrian Research*, *307*, 34–50.

Carlisle, E. M., Jobbins, M., Pankhania, V., Cunningham, J. A., & Donoghue, P. C. (2021). Experimental taphonomy of

organelles and the fossil record of early eukaryote evolution. *Science Advances*, *7*, eabe9487.

Coutant, M., Lepot, K., Fadel, A., Addad, A., Richard, E., Troadec, D., Ventalon, S., Sugitani, K., & Javaux, E. J. (2022). Distinguishing cellular from abiotic spheroidal microstructures in the ca. 3.4 Ga Strelley Pool Formation. *Geobiology*, *20*(5), 599–622.

Czaja, A. D., Beukes, N. J., & Osterhout, J. T. (2016). Sulfur-oxidizing bacteria prior to the great oxidation event from the 2.52 Ga Gamohaan Formation of South Africa. *Geology*, *44*, 983–986.

Dupraz, C., & Visscher, P. T. (2005). Microbial lithification in marine stromatolites and hypersaline mats. *Trends in Microbiology*, *13*(9), 429–438.

El Albani, A., Bengtson, S., Canfield, D. E., Bekker, A., Macchiarelli, R., Mazurier, A., Hammarlund, E. U., Boulvais, P., Dupuy, J. J., Fontaine, C., Fürsich, F. T., Gauthier-Lafaye, F., Janvier, P., Javaux, E., Ossa, F. O., Pierson-Wickmann, A. C., Riboulleau, A., Sardini, P., Vachard, D., … Meunier, A. (2010). Large colonial organisms with coordinated growth in oxygenated environments 2.1 Gyr ago. *Nature*, *466*(7302), 100–104.

El Albani, A., Mangano, M. G., Buatois, L. A., Bengtson, S., Riboulleau, A., Bekker, A., Konhauser, K., Lyons, T., Rollion-Bard, C., Bankole, O., & Lekele Baghekema, S. G. (2019). Organism motility in an oxygenated shallow-marine environment 2.1 billion years ago. *Proceedings of the National Academy of Sciences of the United States of America*, *116*(9), 3431–3436.

Fadel, A., Lepot, K., Busigny, V., Addad, A., & Troadec, D. (2017). Iron mineralisation and taphonomy of microfossils of the 2.45-2.21 Ga Turee Creek Group, Western Australia. *Precambrian Research*, *298*, 530–551.

Francis, S., Margulis, L., & Barghoorn, E. S. (1978). On the experimental silicification of microorganisms II. On the time of appearance of eukaryotic organisms in the fossil record. *Precambrian Research*, *6*(1), 65–100.

Garcia-Pichel, F. (2009). Cyanobacteria. In M. Schaechter (Ed.), *Encyclopedia of microbiology* (Vol. *3*, pp. 107–124). Academic Press.

Garcia-Ruiz, J. M., Hyde, S. T., Carnerup, A. M., Christy, A. G., Van Kranendonk, M. J., & Welham, N. J. (2003). Self-assembled silica-carbonate structures and detection of ancient microfossils. *Science*, *302*, 1194–1197.

Giordano, M., Beardall, J., & Raven, J. A. (2005). CO_2 concentrating mechanisms in algae: Mechanisms, environmental modulation, and evolution. *Annual Review of Plant Biology*, *56*, 99–131.

Gold, D. A., Caron, A., Fournier, G. P., & Summons, R. E. (2017). Paleoproterozoic sterol biosynthesis and the rise of oxygen. *Nature*, *543*, 420–423.

Goldstein, M. (1964). Speciation and mating behavior in Eudorina. *The Journal of Protozoology*, *11*(3), 317–344.

Golubic, S., & Barghoorn, E. S. (1977). Interpretation of microbial fossils with special reference to the Precambrian. In E. Flügel (Ed.), *Fossil algae* (pp. 1–14). Springer.

Golubic, S., & Hofmann, H. J. (1976). Comparison of Holocene and mid-Precambrian Entophysalidaceae (Cyanophyta) in stromatolitic algal mats: Cell division and degradation. *Journal of Paleontology*, *50*(6), 1074–1082.

González-Flores, A. L., Jin, J., Osinski, G. R., & Tsujita, C. J. (2022). Acritarch-like microorganisms from the 1.9 Ga Gunflint chert, Canada. *Astrobiology*, *22*(5), 568–578.

Guasto, J. S., Rusconi, R., & Stocker, R. (2012). Fluid mechanics of planktonic microorganisms. *Annual Review of Fluid Mechanics*, *44*, 373–400.

Han, T. M., & Runnegar, B. (1992). Megascopic eukaryotic algae from the 2.1-billion-year-old Negaunee Iron-Formation, Michigan. *Science*, *257*(5067), 232–235.

Hayes, J. M., Kaplan, I. R., & Wedeking, K. W. (1983). Precambrian organic geochemistry, preservation of the record. In J. W. Schopf (Ed.), *Earth's earliest biosphere* (pp. 93–134). Princeton University Press.

Hayes, J. M., Strauss, H., & Kaufman, A. J. (1999). The abundance of ^{13}C in marine organic matter and isotopic fractionation in the global biogeochemical cycle of carbon during the past 800 Ma. *Chemical Geology*, *161*, 103–125.

Herron, M. D., & Nedelcu, A. M. (2015). Volvocine algae: from simple to complex multicellularity. In I. Ruiz-Trillo & A. M. Nedelcu (Eds.), *Evolutionary transitions to multicellular life* (pp. 129–152). Springer.

House, C. H. (2015). A synthetic standard for the analysis of carbon isotopes of carbon in silicates, and the observation of a significant water-associated matrix effect. *Geochemical Transactions*, *16*, 14.

House, C. H., Schopf, J. W., McKeegan, K. D., Coath, C. D., Harrison, T. M., & Stetter, K. O. (2000). Carbon isotopic composition of individual Precambrian microfossils. *Geology*, *28*, 707–710.

Hugler, M., & Sievert, S. M. (2011). Beyond the Calvin cycle: Autotrophic carbon fixation in the ocean. *Annual Review of Marine Science*, *3*, 261–289.

Igisu, M., Ueno, Y., Shimojima, M., Nakashima, S., Awramik, S. M., Ohta, H., & Maruyama, S. (2009). Micro-FTIR spectroscopic signatures of bacterial lipids in Proterozoic microfossils. *Precambrian Research*, *173*(1–4), 19–26.

Javaux, E. J., Marshall, C. P., & Bekker, A. (2010). Organic-walled microfossils in 3.2-billion-year-old shallow-marine siliciclastic deposits. *Nature*, *463*(7283), 934–938.

Jing, Y., Chen, Z. Q., & Tu, C. (2022). A late Paleoproterozoic microfossil community from siliceous granules, Dahongyu Formation, North China. *Precambrian Research*, *377*, 106723.

John, D. M., Whitton, B. A., & Brook, A. J. (2011). *The freshwater algal flora of the British Isles: An identification guide to freshwater and terrestrial algae*. Cambridge University Press.

Kazmierczak, J., & Kremer, B. (2009). Thermally altered Silurian cyanobacterial mats: A key to Earth's oldest fossils. *Astrobiology*, *9*, 731–743.

Klein, C., Beukes, N. J., & Schopf, J. W. (1987). Filamentous microfossils in the early Proterozoic Transvaal Supergroup: Their morphology, significance, and paleoenvironmental setting. *Precambrian Research*, *36*, 81–94.

Knoll, A. H. (1985). Exceptional preservation of photosynthetic organisms in silicified carbonates and silicified peats. *Philosophical Transactions of the Royal Society of London B*, *311*(1148), 111–122.

Knoll, A. H. (2014). Paleobiological perspectives on early eukaryotic evolution. *Cold Spring Harbor Perspectives in Biology*, *6*, a016121.

Knoll, A. H., & Barghoorn, E. S. (1975). Precambrian eukaryotic organisms: A reassessment of the evidence. *Science*, *190*, 52–54.

Knoll, A. H., & Barghoorn, E. S. (1976). A gunflint-type microbiota from the Duck Creek Dolomite, Western Australia. *Origins of Life*, *7*, 417–423.

Knoll, A. H., & Barghoorn, E. S. (1977). Archean microfossils showing cell division from the Swaziland system of South Africa. *Science*, *198*, 396–398.

Knoll, A. H., Strother, P. K., & Rossi, S. (1988). Distribution and diagenesis of microfossils from the lower Proterozoic Duck Creek Dolomite, Western Australia. *Precambrian Research*, *38*, 257–279.

Komarek, J., & Johansen, J. R. (2015). Coccoid cyanobacteria. In *Aquatic ecology, freshwater algae of North America* (Vol. *2*, pp. 75–133). Academic Press.

Krapez, B., Müller, S. G., Fletcher, I. R., & Rasmussen, B. (2017). A tale of two basins? Stratigraphy and detrital zircon provenance of the Palaeoproterozoic Turee Creek and Horseshoe basins of Western Australia. *Precambrian Research*, *294*, 67–90.

Manning-Berg, A., Selly, T., & Bartley, J. K. (2022). Actualistic approaches to interpreting the role of biological decomposition in microbial preservation. *Geobiology*, *20*(2), 216–232.

Margulis, L., & Chapman, M. J. (2009). *Kingdoms and domains: An illustrated guide to the phyla of life on Earth* (4th ed.). Academic Press.

Martin, D. M. (2020). *Geology of the Hardey Syncline—The key to understanding the northern margin of the Capricorn rogen*. Geological Survey of Western Australia, report 203.

Martin, D. M., Li, Z. X., Nemchin, A. A., & Powell, C. M. (1998). A pre-2.2 Ga age for giant hematite ores of the Hamersley Province, Australia? *Economic Geology*, *93*, 1084–1090.

Matthews, R. A. (2016). Freshwater algae in Northwest Washington, volume II, Chlorophyta and Rhodophyta. In *Books and monographs, book 1*. Western Washington University. https://cedar.wwu.edu/cedarbooks/1/

McCollom, T. M., Ritter, G., & Simoneit, B. R. T. (1999). Lipid synthesis under hydrothermal conditions by Fischer-Tropsch-type reactions. *Origins of Life and Evolution of the Biosphere*, *29*, 153–166.

Menezes, M., & Bicudo, C. E. M. (2008). Flagellate green algae from four water bodies in the state of Rio de Janeiro, Southeast Brazil. *Hoehnea*, *35*, 435–468.

Miao, L., Moczydlowska, M., Zhu, S., & Zhu, M. (2019). New record of organic-walled, morphologically distinct microfossils from the late Paleoproterozoic Changcheng Group in the Yanshan Range, North China. *Precambrian Research*, *321*, 172–198.

Moczydłowska, M., & Willman, S. (2009). Ultrastructure of cell walls in ancient microfossils as a proxy to their biological affinities. *Precambrian Research*, *173*(1–4), 27–38.

Moore, K. R., Gong, J., Pajusalu, M., Skoog, E. J., Xu, M., Feliz Soto, T., Sojo, V., Matreux, T., Baldes, M. J., Braun, D., & Williford, K. (2021). A new model for silicification of cyanobacteria in Proterozoic tidal flats. *Geobiology*, *19*(5), 438–449.

Moorman, M. (1974). Microbiota of the late Proterozoic Hector Formation, southwestern Alberta. *Canadian Journal of Paleontology*, *48*, 524–539.

Muñoz-Dorado, J., Marcos-Torres, F. J., García-Bravo, E., Moraleda-Muñoz, A., & Pérez, J. (2016). Myxobacteria: Moving, killing, feeding, and surviving together. *Frontiers in Microbiology*, *7*, 781.

Nagovitsin, K. (2009). Tappania-bearing association of the Siberian platform: Biodiversity, stratigraphic position and geochronological constraints. *Precambrian Research*, *173*(1–4), 137–145.

Nakada, T., & Nozaki, H. (2015). Flagellate green algae. In J. D. Wehr, R. G. Sheath, & J. P. Kociolek (Eds.), *Aquatic ecology, freshwater algae of North America* (2nd ed., pp. 265–313). Academic Press.

Nomchong, B. (2021). Depositional and diagenetic environment of a c. 2.4 Ga microbialite reef complex from the Turee Creek Group, Western Australia. PhD thesis, University of New South Wales, Sydney, 439 p.

Nomchong, B. J., & Van Kranendonk, M. J. (2020). Diverse thrombolites from the c. 2.4 Ga Turee Creek Group, Western Australia. *Precambrian Research*, *338*, 105593.

Nozaki, H., Yamada, T. K., Takahashi, F., Matsuzaki, R., & Nakada, T. (2014). New "missing link" genus of the colonial volvocine green algae gives insights into the evolution of oogamy. *BMC Evolutionary Biology*, *14*, 1–11.

Oehler, D. Z., Walsh, M. M., Sugitani, K., Liu, M. C., & House, C. H. (2017). Large and robust lenticular microorganisms on the young Earth. *Precambrian Research*, *296*, 112–119.

Oehler, J. H. (1976). Hydrothermal crystallization of silica gel. *Geological Society of America Bulletin*, *87*, 1143–1152.

Onuoha, P. C., Nwankwo, D. I., & Vyverman, W. (2010). A checklist of phytoplankton species of Ologe lagoon, Lagos south-estern Nigeria. *Journal of American Science*, *6*(9), 297–302.

Palacios, T., Jensen, S., White, C. E., & Barr, S. M. (2012). Cambrian acritarchs from the Bourinot belt, Cape Breton Island, Nova Scotia: Age and stratigraphic implications. *Canadian Journal of Earth Sciences*, *49*, 289–307.

Parfrey, L. W., Lahr, D. J. G., Knoll, A. H., & Katz, L. A. (2011). Estimating the timing of early eukaryotic diversification with multigene molecular clocks. *Proceedings of the National Academy of Sciences of the United States of America*, *108*, 13624–13629.

Pentecost, A. (2011). Order Volvocales. In D. M. John, B. A. Whitton, & A. J. Brook (Eds.), *The freshwater algal flora of the British Isles: An identification guide to freshwater and terrestrial algae* (pp. 381–410). Cambridge University Press.

Philippot, P., Avila, J. N., Killingsworth, B. A., Tessalina, S., Baton, F., Caquineau, T., Muller, E., Pecoits, E., Cartigny, P., Lalonde, S. V., & Ireland, T. R. (2018). Globally asynchronous sulphur isotope signals require re-definition of the great oxidation event. *Nature Communications*, *9*, 2245.

Prescott, G. W. (1955). Algae of the Panama Canal and its tributaries: I flagellated organisms. *Ohio Journal of Science*, *55*, 99–121.

Preuss, A., Schauder, R., Fuchs, G., & Stichler, W. (1989). Carbon isotope fractionation by autotrophic bacteria with three different CO_2 fixation pathways. *Zeitschrift für Naturforschung*, *44*, 397–402.

Rasmussen, B., Muhling, J. R., & Fischer, W. W. (2021). Ancient oil as a source of carbonaceous matter in 1.88-billion-year-old Gunflint stromatolites and microfossils. *Astrobiology*, *21*, 655–672.

Reynolds, C. S. (1984). *The ecology of freshwater phytoplankton*. Cambridge University Press.

Riley, G. A. (1971). Particulate organic matter in sea water. In F. S. Russell & M. Yonge (Eds.), *Advances in marine biology* (Vol. *8*, pp. 1–118). Academic Press.

Roeske, C. A., & O'Leary, M. H. (1984). Carbon isotope effects on the enzyme-catalyzed carboxylation of ribulose bisphosphate. *Biochemistry*, *23*, 6275–6284.

Sasaki, K., Ishida, A., Takahata, N., Sano, Y., & Kakegawa, T. (2022). Evolutionary diversification of paleoproterozoic prokaryotes: New microfossil records in 1.88 Ga Gunflint Formation. *Precambrian Research*, *380*, 106798.

Schopf, J. W. (1993). Microfossils of the early Archean Apex chert: New evidence of the antiquity of life. *Science*, *260*(5108), 640–646.

Schopf, J. W., Kudryavtsev, A. B., Walter, M. R., Van Kranendonk, M. J., Williford, K. H., Kozdon, R., Valley, J. W., Gallardo, V. A., Espinoza, C., & Flannery, D. T. (2015). Sulfur-cycling fossil bacteria from the 1.8-Ga Duck Creek Formation provide promising evidence of evolution's null hypothesis. *Proceedings of the National Academy of Sciences of the United States of America*, *112*, 2087–2092.

Sergeev, V. N. (1994). Microfossils in cherts from the middle Riphean (Mesoproterozoic) Avzyan Formation, southern Ural Mountains, Russian Federation. *Precambrian Research*, *65*(1–4), 231–254.

Smith, R. E., Perdrix, J. L., & Parks, T. C. (1982). Burial metamorphism in the Hamersley Basin, Western Australia. *Journal of Petrology*, *23*, 75–102.

Soares, G. G., Van Kranendonk, M. J., Belousova, E., & Thomson, S. (2019). Phosphogenesis in the immediate aftermath of the great oxidation event: Evidence from the Turee Creek Group, Western Australia. *Precambrian Research*, *320*, 193–212.

Sugitani, K., Lepot, K., Nagaoka, T., Mimura, K., Van Kranendonk, M., Oehler, D. Z., & Walter, M. R. (2010). Biogenicity of morphologically diverse carbonaceous microstructures from the ca. 3400 Ma Strelley Pool Formation, in the Pilbara craton, Western Australia. *Astrobiology*, *10*(9), 899–920.

Sugitani, K., Mimura, K., Takeuchi, M., Lepot, K., Ito, S., & Javaux, E. J. (2015). Early evolution of large microorganisms with cytological complexity revealed by microanalyses of 3.4 Ga organic-walled microfossils. *Geobiology*, *13*, 507–521.

Thorne, A. M., & Tyler, I. M. (1996). Geology of the Rocklea 1:100 000 sheet. Western Australia Geological Survey. 1:100 000 geological series explanatory notes.

Walsh, M. M., & Lowe, D. R. (1985). Filamentous microfossils from the 3,500-Myr-old Onverwacht Group, Barberton Mountain Land, South Africa. *Nature*, *314*, 530–532.

Whitton, B. A. (2011). Phylum cyanobacteria (Cyanophyta). In D. M. John, B. A. Whitton, & A. J. Brook (Eds.), *The freshwater algal flora of the British Isles: An identification guide to freshwater and terrestrial algae* (pp. 31–158). Cambridge University Press.

Williford, K. H., Ushikubo, T., Schopf, J. W., Lepot, K., Kitajima, K., & Valley, J. W. (2013). Preservation and detection of microstructural and taxonomic correlations in the carbon isotopic compositions of individual Precambrian microfossils. *Geochimica et Cosmochimica Acta*, *104*, 165–182.

Williford, K. H., Van Kranendonk, M. J., Ushikubo, T., Kozdon, R., & Valley, J. W. (2011). Constraining atmospheric oxygen and seawater sulfate concentrations during Paleoproterozoic glaciation: In situ sulfur three isotope microanalysis of pyrite from the Turee Creek Group, Western Australia. *Geochimica et Cosmochimica Acta*, *75*, 5686–5705.

Xiao, M., Li, M., & Reynolds, C. S. (2018). Colony formation in the cyanobacterium microcystis. *Biological Reviews*, *97*, 1399–1420.

Xiao, M., Willis, A., Burford, M. A., & Li, M. (2017). Review: A meta-analysis comparing cell-division and cell adhesion in Microcystis colony formation. *Harmful Algae*, *67*, 85–91.

Xiao, S., Yuan, X., & Knoll, A. H. (2000). Eumetazoan fossils in terminal Proterozoic phosphorites? *Proceedings of the National Academy of Sciences of the United States of America*, *97*(25), 13684–13689.

Yamada, T. K., Miyaji, K., & Nozaki, H. (2008). A taxonomic study of Eudorina unicocca (Volvocaceae, Chlorophyceae) and related species, based on morphology and molecular phylogeny. *European Journal of Phycology*, *43*, 317–326.

Yin, L. M., Wang, K., Shen, Z., & Zhao, Y. L. (2021). Organic-walled microfossils from Cambrian stage IV in the Jiaobang section, eastern Guizhou, China. *Palaeoworld*, *30*(3), 398–421.

SUPPORTING INFORMATION

Additional supporting information can be found online in the Supporting Information section at the end of this article.

How to cite this article: Barlow, E. V., House, C. H., Liu, M.-C., Wetherington, M. T., & Van Kranendonk, M. J. (2023). Distinctive microfossil supports early Paleoproterozoic rise in complex cellular organisation. *Geobiology*, *00*, 1–23. https://doi.org/10.1111/gbi.12576